Computers and Geotechnics 137 (2021) 104275

Contents lists available at ScienceDirect

Computers and Geotechnics

journal homepage: www.elsevier.com/locate/compgeo

Modelling the wave-induced instantaneous liquefaction in a non-cohesive seabed as a nonlinear complementarity problem

Mozhen Zhou [a], Hui Liu [b], Dong-Sheng Jeng [c], Wengang Qi [d,e,*], Qian Fang [a]

[a] Key Laboratory for Urban Underground Engineering of the Ministry of Education, Beijing Jiaotong University, 100044 Beijing, China
[b] China Institute of Water Resources and Hydropower Research, Beijing 100038, China
[c] School of Engineering & Built Environment, Griffith University Gold Coast Campus, Queensland 4222, Australia
[d] Key Laboratory for Mechanics in Fluid Solid Coupling Systems, Institute of Mechanics, Chinese Academy of Sciences, Beijing 100190, China
[e] School of Engineering Science, University of Chinese Academy of Sciences, Beijing 100049, China

ARTICLE INFO

Keywords:
Nonlinear complementarity problem
Karush–Kuhn–Tucker (KKT) condition
Lagrange multiplier method
Soil liquefaction
Wave-seabed interactions

ABSTRACT

The estimation of the wave-induced instantaneous liquefaction is particularly important for the design of foundations of offshore structures. Regarding the occurrence of liquefaction in a non-cohesive seabed, most existing studies using constant permeability were found to cause fallacious tensile stresses in the liquefied zone and further pollute the overall pore pressure distribution. A dynamic permeability model was previously presented to mitigate the shortcoming but posed difficulties in the nonlinear convergence. To overcome the shortcoming of the previous studies, this study proposes the concept of modelling the liquefaction-involved wave-seabed interactions as a nonlinear complementarity problem, wherein a Karush–Kuhn–Tucker condition is constructed, based on revisiting the liquefaction criterion most widely applied in ocean engineering. The Lagrange multiplier method and the primal–dual active set strategy are employed to numerically deal with the nonlinear complementarity problem. The performance of the chosen multiplier space is investigated by theoretical analyzing and numerical modelling. Compared with the previous dynamic permeability model, the present model is totally free of extra parameters and precisely fulfills the no-tension requirement. Moreover, the difficulties of dynamic permeability in the nonlinear convergence are overcome and no divergence is observed in the numerical tests.

1. Introduction

The phenomenon of liquefaction in porous medium is one of the most challenging issues for offshore geotechnics. This study focuses on the wave-induced instantaneous liquefaction in a non-cohesive seabed, due to the following three considerations. First, this scenario is of profound interest to engineers due to the wide applications in ocean engineering, such as offshore wind turbine foundations (Qi and Gao, 2014; Sui et al., 2016; Lin et al., 2017), submarine pipelines (Li et al., 2019; Liang et al., 2020), breakwaters (Zhang et al., 2018; Celli et al., 2019) and immersed tunnel (Chen et al., 2019; Han et al., 2019) etc. The present study focusing on the wave-seabed interactions is fundamental for a potential extension to wave-seabed-structure interactions. Second, if the soil is liquefied, the large deformation of the seabed may accelerate the damage cause by other seabed instability such as scouring (Tonkin et al., 2003; Yeh and Mason, 2014; Abdollahi and Mason, 2020). For these complicated scenarios, this study is envisioned to provide a basis/onset for applying continuum-discontinuum combined methods in the future to accomplish a whole-process simulation. Third, this scenario has relatively naive behaviors and therefore is convenient enough for numerical and mechanism explorations, which are discussed in detail as below.

The naturally deposited seabed sand is commonly in a loose state with low bearing capacity and high liquefaction potential under cyclic wave loading. After a long period of 'wave-induced compaction or solidation' (Miyamoto et al., 2004; Sumer et al., 2006; Sumer, 2014), the loose soil will be rearranged to a dense state by squeezing out the pore-fluid. Thereafter, further soil compaction accompanied by the plastic

* Corresponding author at: Key Laboratory for Mechanics in Fluid Solid Coupling Systems, Institute of Mechanics, Chinese Academy of Sciences, Beijing 100190, China.
E-mail addresses: mzzhou@bjtu.edu.cn (M. Zhou), wuyouliuhui@163.com (H. Liu), d.jeng@griffith.edu.au (D.-S. Jeng), qiwengang@imech.ac.cn (W. Qi), qfang@bjtu.edu.cn (Q. Fang).

https://doi.org/10.1016/j.compgeo.2021.104275
Received 22 October 2020; Received in revised form 26 May 2021; Accepted 28 May 2021
Available online 12 June 2021

volumetric deformation is unlikely to occur under historical dynamic loading, making the dense seabed suitable for installing offshore foundations. For the seabed being sufficiently densified by 'wave-induced compaction', the instantaneous liquefaction associated with wave-induced transient pore pressure becomes a major concern (Sumer and Fredsøe, 2002; Jeng, 2012). On the other hand, the sufficiently compacted state makes the subsequent wave loading fall into the reloading–unloading stage of the seabed. Therefore, the poro-elastic theory can be adopted when considering the transient pore pressure response and associated instantaneous liquefaction (Jeng, 2012). Based on simplified assumptions of soil behavior and environmental loading, the wave-induced transient pore pressure response has been analytically investigated under various conditions, e.g. isotropic seabed with infinite thickness (Yamamoto et al., 1978), hydraulically anisotropic seabed with infinite thickness (Madsen, 1978), isotropic seabed with finite soil thickness (Hsu and Jeng, 1994), infinite thick isotropic seabed under combined waves and a current (Zhang et al., 2013), etc.

It should be noted that there is another type of wave-induced seabed liquefaction, i.e. residual liquefaction caused by the residual (or accumulated) pore pressure (Sumer and Fredsøe, 2002; Jeng, 2012). The residual liquefaction is most likely to occur in loose to medium dense sands or silts. In this case, there are generally two kinds of treatments used in numerical simulations, i.e. introducing source terms into the governing equations (Seed et al., 1976; Seed and Rahman, 1978; Jeng et al., 2007; Sumer et al., 2012; Jeng and Zhao, 2015) or adopting nonlinear constitutive relations (e.g. elasto-plasticity (Sassa and Sekiguchi, 2001; Jeng and Ou, 2010; Wang et al., 2014; Ye et al., 2015; Elsafti and Oumeraci, 2016)). It has been well known that transient mechanism can be described by poro-elastic models, while residual mechanism requires poro-elastoplastic models (Jeng, 2012). In this study, we focus on the instantaneous liquefaction. The extensions to residual liquefaction will be discussed in our future works.

In existing models for wave-seabed interactions, the pore-fluid flow in the porous seabed is generally characterized by the linear Darcy's law. For the instantaneous liquefaction, Wu and Jeng (2019) was the first considering the soil permeability k being a function of the pore pressure p. This dynamic permeability model was further extended to consider dynamic saturation degree for consolidation-induced contaminate transport (Wu et al., 2020). However, the dynamic permeability model (Wu and Jeng, 2019) was found to cause an apparent decrease of the soil permeability in the liquefied zone, disagreeing with increased permeability during soil liquefaction observed in experiments (Arulanandan and Sybico, 1992; Ha et al., 2003; Haigh et al., 2012; Wang et al., 2013; Shahir et al., 2014; Ueng et al., 2017). This issue was addressed in Zhou et al. (2020b), wherein the permeability increase during soil liquefaction is characterized by a new k-p relation. Furthermore, the new k-p relation alleviates the disadvantage of the conventional constant permeability model of causing tensile stresses, which are fallacious in physics and should not occur in a non-cohesive seabed (Qi and Gao, 2015; Qi and Gao, 2018). Nevertheless, the nonlinear convergence performance of the previous model with dynamic permeability (Zhou et al., 2020b) was found to be poor. Numerical divergence can even occur when simulating the seabed under two-dimensional (2D) wave loading conditions. To obtain converged solutions, the model parameters in Zhou et al. (2020b) were chosen in such a way that the nonlinearity is not too strong to break down the numerical procedure. This eclectic choice leads to a consequence that the non-physical tensile behavior can only be partially eased rather than totally eliminated. Therefore, a novel treatment is still in need.

The present model treats the liquefaction problem in physics as a nonlinear complementarity problem (NCP) in mathematics. It is notable that there exist several works using NCP to model other complex physical problems, e.g. the static growth of multiple cracks (Zheng et al., 2015) and the non-associative plasticity with non-smooth yield surfaces (Zheng et al., 2020). It was found that the complexity for numerical and theoretical analyses can be reduced owing to the use of NCP. In this study, the NCP is presented by constructing a Karush–Kuhn–Tucker (KKT) condition specified for instantaneous liquefaction. Noting that KKT condition has been used in computational contact mechanics (Wriggers, 2006), it is therefore straightforward for us to borrow ideas from numerical contact methods to deal with the KKT condition constructed here. In the present model, the KKT condition is imposed by the Lagrange multiplier method and is iteratively solved by the primal–dual active set strategy (Kunisch and RöSch, 2002). For the saddle-point system arising from the Lagrange multiplier method, the computational efficiency is guaranteed by using the Direct delta function to interpolate the multipliers which can therefore be statically condensed. The NCP treatment proposed in the present model has several advantages over the dynamic permeability model by Zhou et al. (2020b). First, the proposed NCP treatment can totally eliminate the tensile behavior and at the same time overcomes the difficulties in the nonlinear convergence. Second, the NCP treatment is free of extra parameters, making the formulation elegant and clean. Third, NCP provides a numerical framework which is convenient for introducing other state-of-the-art methods (e.g. cut-cell quadrature and semi-smooth Newton method) in the future to further improve the numerical performance.

It should be noted that elasto-plasticity models (Sassa and Sekiguchi, 2001; Jeng and Ou, 2010; Wang et al., 2014; Ye et al., 2015; Elsafti and Oumeraci, 2016) for residual liquefaction can be also adopted to address the tensile behavior issue occurring in conventional models for instantaneous liquefaction. Within these elasto-plasticity models, the soil moduli is generally taken as a small value when liquefaction occurs, noting that zero-value soil moduli can lead to an ill condition or singularity of the global matrix system. This treatment can reproduce the loss of solid-phase resistance during liquefaction (Haigh et al., 2012; Adamidis and Madabhushi, 2016) and hence fulfill the non-tension requirement in an approximate manner. In contrast, the present model can fulfill the non-tension requirement in a precise manner, as demonstrated in Sections 5 and 6. The main limitation of the present model is that the NCP treatment is incorporated into the poro-elastic theory and hence is insufficient to model residual liquefaction. The NCP treatment is envisioned to be extended to elasto-plasticity models in the future and thus residual liquefaction can be modelled with reproducing real soil characteristics and meanwhile totally eliminating the tensile behavior.

The remaining sections of this paper are organized as follows. Section 2 briefly outlines the fundamental theory and governing equations for wave-seabed interactions. In Section 3, the most widely applied criterion for determining the liquefaction potential in ocean engineering is revisited and then the pore pressure constraints are proposed to directly fulfill the no-tension requirement. The weak form and discretization of the resultant constrained system are deduced with the use of the Lagrange multiplier method. The choice of the discrete multiplier space is also discussed. Section 4 completes the description by finding the additional dual and complementarity condition and then provides the iterative procedure for the resultant NCP. The superior performances of the proposed approach are confirmed by numerical examples in Sections 5 and 6. Finally, several key conclusions are drawn in Section 7.

2. Boundary value problem for wave-seabed interactions

The boundary value problem presented in this section can be also found in Jeng (2012) and has been widely applied in marine geotechnics. To provide some necessary bases for Sections 3 and 4 wherein our key contributions will be proposed, here we try to present the fundamental theory in a concise way without losing rigorousness in mathematics.

Fig. 1 shows a 2D problem for wave-seabed interactions, with the seabed thickness (d), the water depth (h), and the wave height (H). Note that the effects of wave non-linearity on the seabed responses could be non-negligible for large waves in shallow water. In those cases, the nonlinear wave pressure induced by Stokes wave (e.g. Gao et al., 2003) or cnoidal wave (e.g. Zhou et al., 2014) needs to be taken into account. For

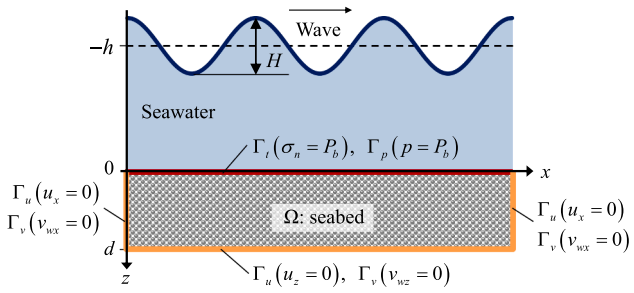

Fig. 1. Schematic of the wave-seabed interactions.

the sake of simplicity and highlighting the key contribution, the linear wave theory is used in this study. The non-cohesive seabed body (Ω) is under the assumption of porous medium. The z axis is defined as downward such that z equals to zero at the seabed surface and deeper positions have positive values.

The poro-elastic theory (Biot, 1941) is adopted for the wave-seabed interactions. The boundary value problem of the seabed model can be written as follows:

$$\nabla\cdot(\boldsymbol{\sigma}' - p\mathbf{I}_{2\times 2}) + \mathbf{b} = 0 \quad \text{in} \quad \Omega, \tag{1a}$$

$$\frac{\partial \varepsilon_v}{\partial t} + n\beta\frac{\partial p}{\partial t} - \nabla\cdot\left(\frac{k}{\gamma_w}\nabla p\right) = 0, \quad \text{in} \quad \Omega, \tag{1b}$$

$$\mathbf{u} = \widehat{\mathbf{u}}, \quad \text{on} \quad \Gamma_u, \tag{1c}$$

$$p = \widehat{p}, \quad \text{on} \quad \Gamma_p, \tag{1d}$$

$$\boldsymbol{\sigma}\cdot\mathbf{n}^N = \widehat{\mathbf{t}}, \quad \text{on} \quad \Gamma_t, \tag{1e}$$

$$\mathbf{v}_w\mathbf{n}^N = \widehat{v}_w^n, \quad \text{on} \quad \Gamma_v. \tag{1f}$$

In the above boundary value problem, Eq. (1a) represents the equilibrium of the solid–fluid mixture, with the effective stress ($\boldsymbol{\sigma}'$), the wave-induced excessive pore pressure (p), a second-order unit tensor ($\mathbf{I}_{2\times 2}$) and the body force per unit volume ($\mathbf{b}$). Eq. (1b) establishes the conservation of mass, with the volumetric strain (ε_v), time t, soil porosity (n), pore fluid compressibility (β), Darcy's coefficient of permeability (k) and weight of water per unit volume (γ_w). The latter four equalities in Eq. (1) represent the boundary conditions, which are divided into four open subsets, as shown in Fig. 1. Γ_u and Γ_p are Dirichlet boundaries for solid and fluid phases, respectively. Γ_t and Γ_v are Neumann boundaries for solid and fluid phases, respectively. $\mathbf{u}$ is the displacement vector and $\boldsymbol{\sigma}$ is the total stress tensor. $\mathbf{n}^N$ is the outward unit normal vector on the boundary and $\mathbf{v}_w$ is the pore-fluid velocity vector. $\widehat{\mathbf{u}}, \widehat{p}, \widehat{\mathbf{t}}$ and $\widehat{v}_w^n$ are the constrained displacement, constrained pore pressure, boundary traction and boundary Darcy velocity, respectively.

The pore-fluid flow in porous media is assumed to obey the Darcy's law wherein the pore-fluid velocity ($\mathbf{v}_w$) is given by a linear function of the hydraulic gradient:

$$\mathbf{v}_w = \frac{k}{\gamma_w}\nabla p. \tag{2}$$

The compressibility of pore-fluid (β) is determined by (Verruijt, 1969):

$$\beta = \frac{1}{K_{w0}} + \frac{1 - S_r}{P_{\text{abs}}}, \tag{3}$$

where K_{w0} is the true bulk modulus of pore water and taken as 2.0×10^9 Pa (Yamamoto et al., 1978). S_r is the degree of saturation. The absolute water pressure P_{abs} denotes the local static pore pressure in the seabed, which is commonly calculated by $P_{\text{abs}} = \gamma_w h$.

For the 2D case, the four types of boundary conditions are illustrated in Fig. 1. On the bottom and both sides of the seabed, the displacement and pore-fluid flow along the normal direction are constrained as zero. At the seabed surface, the pore pressure of the fluid phase is constrained as a time-dependent wave pressure P_b, and P_b is also applied as a distributed pressure to the solid phase. The wave pressure P_b is determined in this work by the linear wave theory (Dean and Dalrymple, 1984):

$$P_b = p_0\cos(k_w x - \omega t), \tag{4a}$$

$$p_0 = \frac{\gamma_w H}{2\cosh(k_w h)}, \quad \omega = \frac{2\pi}{T}, \quad k_w = \frac{2\pi}{L}, \tag{4b}$$

with the pressure amplitude (p_0) on the seabed surface, the wave angular frequency (ω), wave period (T), wave number (k_w) and wavelength (L). The wavelength L is determined by the wave dispersion relation:

$$L = \frac{gT^2}{2\pi}\tanh\left(\frac{2\pi}{L}h\right), \tag{5}$$

where g is the acceleration of gravity.

It should be noted that the boundary conditions may become more complicated in more general scenarios, e.g. when an offshore structure is considered. The early numerical studies mainly paid attention to the pore pressure response in the vicinity of a 'fixed' buried pipeline (Jeng and Lin, 1999; Gao et al., 2003). In these works, the effect of the waves on the porous seabed domain was simplified as formulated pressure fluctuations acting on the seabed surface, and therefore only the governing equations of a porous seabed domain need to be considered. These treatments are identical to Eq. (1) for the case without a structure. The difference is that the structure-seabed interaction should be further modelled. Recent interests have been attracted to cases with structures inserting into both fluid and seabed domains, e.g., partially-buried pipelines (Zhao and Jeng, 2016; Duan et al., 2017), monopile foundations (Sui et al., 2016; Lin et al., 2017) and gravity foundations for offshore wind turbines (OWTs) (Li et al., 2018). Due to the existence of wave-structure interactions, the wave pressure distribution at the seabed surface needs to be determined via advanced hydrodynamic models instead of simplified pressure fluctuations (Liang et al., 2020).

Moreover, some previous experimental studies showed that the structure rocking motion induced by cyclic loading can generate excess pore pressure in the vicinity of the structure (Kudella et al., 2006; Sumer et al., 2008). This rocking effect was investigated by Cuéllar et al. (2014) and Liao et al. (2019). If the environmental loads (e.g. the thermal-expansion-induced uplift force on a buried pipeline or the wind load on a monopile foundation for OWTs) need to be further considered, the discontinuous deformation at the structure-seabed interface can be large and therefore an appropriate nonlinear contact method is required. On this topic, Chen et al. (2019) and Qi et al. (2020) investigated the uplift bearing capacity of a buried pipeline influenced by residual and transient pore pressures, respectively. It can be concluded that a generic model for wave-structure-seabed interactions should appropriately incorporate the soil constitutive model, the seawater hydrodynamic model and interactions at three interfaces (i.e. wave–seabed, wave–structure and structure–seabed). The present study focuses on the case of wave–seabed interactions without a structure, which has a fundamental significance for future extensions considering offshore foundations.

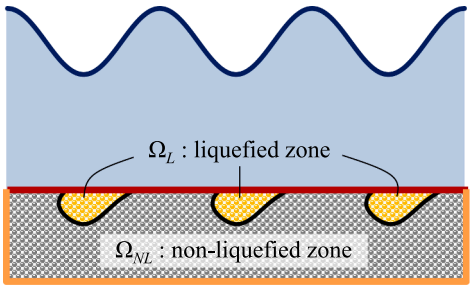

Fig. 2. Schematic of the liquefied and non-liquefied zones.

3. The constrained system arising from the liquefaction criterion

3.1. Pore pressure constraints by revisiting the liquefaction criterion

As shown in Fig. 2, the instantaneously liquefied zone is denoted by Ω_L. The non-liquefied zone is denoted by Ω_{NL}. Ω_L and Ω_{NL} fulfill the following relation:

$$\Omega_L \cap \Omega_{NL} = \varnothing, \ \Omega_L \cup \Omega_{NL} = \Omega, \tag{6}$$

In this study, we limit our focus on the framework of a continuum-based method, i.e., the finite element method based on Biot's theory. The main contribution of the present work is the improvement of the numerical modelling and to make the theory self-consistent, i.e. fulfilling the no-tension requirement in a non-cohesive seabed. Therefore, When liquefaction occurs, Eq. (1) is still used here, but with additional criteria to determining Ω_L. The most widely applied criterion in ocean engineering is the one deduced by Zen and Yamazaki (1990):

$$p - P_b \geqslant \gamma' z, \tag{7}$$

where $\gamma' z$ represents the initial value of the vertical effective stress. The buoyant unit weight γ' can be determined by $\gamma' = (G_s - 1)(1 - n)\gamma_w$, with G_s denoting the specific gravity of sand particles. n is the porosity of the sand: $n = e/(1 + e)$, in which e is the void ratio of the sand, i.e. the ratio of the volume of voids to the volume of solid particles.

The liquefaction criterion by Eq. (7) is based on the force analysis on the vertical soil column. When a wave trough arrives, p and P_b are both negative. If their difference $p - P_b$ becomes greater than the overburden soil pressure $\gamma' z$, instantaneous liquefaction can occur. This criterion was later extended to a three-dimensional condition by Jeng (1997). Here we try to use Fig. 3 to present an intuitive explanation for Eq. (7), which can then provide convenience for the discussion hereafter.

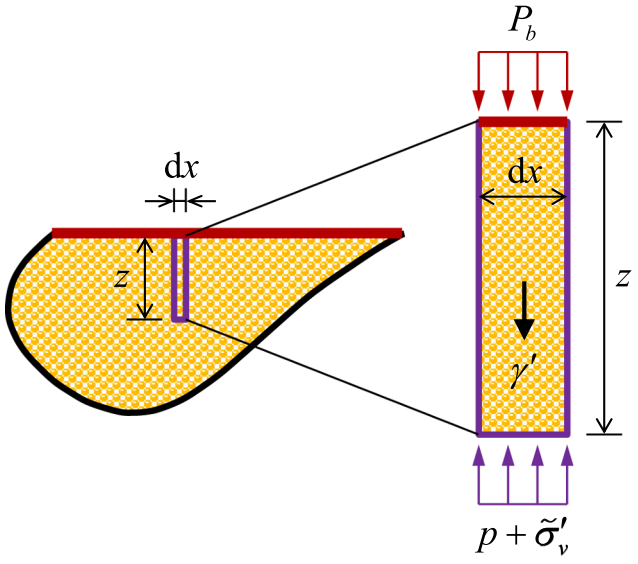

Fig. 3. Physical explanation of the liquefaction criterion by Eq. (7).

In Fig. 3, the vertical soil column from the seabed surface to the specific depth z is considered. The horizontal width is denoted by dx to keep in mind that the soil column width is infinitesimal. There are four types of loading conditions imposed on the soil column: the pressure P_b on the seabed surface, the submerged weight (represented by the body force γ'), and two pressures on the bottom surface coming from the underlying seabed. These two pressures are the wave-induced excess pore pressure p from the fluid phase and the vertical effective stress $\tilde{\sigma}'_v$ from the solid phase. The force balance can then be written as follows:

$$\left(p + \tilde{\sigma}'_v\right)\mathrm{d}x - P_b \mathrm{d}x - \gamma' z \mathrm{d}x = 0 \ \Leftrightarrow \ \tilde{\sigma}'_v = \gamma' z \ - (p - P_b), \tag{8}$$

where the positive value of $\tilde{\sigma}'_v$ represents compression and negative value represents tension. It is easy to find that Eq. (7) is equal to $\tilde{\sigma}'_v \leqslant 0$, i.e., tensile behavior occurs. However, it was concluded by Qi and Gao (2018) that tensile behavior should not occur in a non-cohesive seabed. In Zhou et al. (2020b), the tensile behavior is indirectly eased by using dynamic permeability. Herein, non-tensile requirement is directly fulfilled by introducing the following constraint to the liquefied zone Ω_L:

$$\tilde{\sigma}'_v = 0 \quad \text{or equally} \quad p - P_b - \gamma' z = 0 \ (\text{in } \Omega_L). \tag{9}$$

Note that $\tilde{\sigma}'_v$ can be also interpreted as the contact pressure across the non-cohesive interface between the chosen soil column and the underlying seabed. The no-tension requirement by Eq. (9) can be therefore interpreted by contact mechanics as that tension is not permitted at a non-cohesive interface. It is also notable that the contact interface mentioned here is associated with the coordinate z and z is arbitrary, $\tilde{\sigma}'_v$ is actually defined everywhere in the whole domain Ω. This feature is different from multi-body contact problems wherein the contact interfaces are generally the outer boundaries. Moreover, the no-tension constraint is treated as the dual condition in contact mechanics but is written as a primal condition ($p - P_b - \gamma' z = 0$) here for the wave-seabed interactions. This can be regarded as another distinguishing feature in the instantaneous liquefaction problem. Or in other words, we can physically explain the liquefaction criterion by borrowing the idea from contact mechanics but the numerical treatment here is different from numerical contact methods.

Another issue associated with $\tilde{\sigma}'_v$ is that $\tilde{\sigma}'_v$ differs from σ'_z. $\tilde{\sigma}'_v$ is used here to represent the vertical effective stress defined in Fig. 3 and Eq. (8). However, σ'_z is commonly used to denote the vertical normal component of the effective stress tensor $\boldsymbol{\sigma}'$, which is obtainable from Eq. (1) and dose not include the geostatic stress. The differences between $\tilde{\sigma}'_v$ and σ'_z are highly relevant to two liquefaction criteria. One was deduced by Zen and Yamazaki (1990) and has been given by Eq. (7), which can be rewritten as: $\tilde{\sigma}'_v \leqslant 0$. The other was presented by Okusa (1985) and can be written as: $\gamma' z - \sigma'_z \leqslant 0$, where the positive value of σ'_z represents tension and negative value represents compression. Detailed discussions about different liquefaction criteria can be found in existing works (e.g. Jeng (1997, 2012)) and hence are omitted here.

3.2. Weak form of the constrained system

For the constrained system composed of Eqs. (1) and (9), the constrained variational principle can be used to obtain the weak form. In this study, we apply the Lagrange multiplier method, wherein the Lagrange multiplier λ is introduced as an additional unknown field.

The trial and weighting spaces are defined as:

$$\mathscr{V}_u = \left\{ \mathbf{u} \in \left[H^1(\Omega)\right]^3 \middle| \mathbf{u}|_{\Gamma_u} = \widehat{\mathbf{u}} \right\}, \quad \mathscr{V}_\Phi = \left\{ \Phi \in \left[H^1(\Omega)\right]^3 \middle| \Phi|_{\Gamma_u} = \mathbf{0} \right\}, \tag{10a}$$

$$\mathscr{V}_p = \left\{ p \in \left[H^1(\Omega)\right] \middle| p|_{\Gamma_p} = \widehat{p} \right\}, \quad \mathscr{V}_\phi = \left\{ \phi \in \left[H^1(\Omega)\right] \middle| \phi|_{\Gamma_p} = 0 \right\}, \tag{10b}$$

$$\mathscr{V}_\lambda = \left\{ \lambda \in \left[H^1(\Omega)\right] \middle| \lambda|_{\Omega_{NL}} = 0 \right\}, \quad \mathscr{V}_w = \left\{ w \in \left[H^1(\Omega)\right] \middle| w|_{\Omega_{NL}} = 0 \right\}, \tag{10c}$$

where H^1 denotes a Sobolev space of degree one. Φ, ϕ and w denote the variations of the displacement $\mathbf{u}$, pore pressure p and Lagrange multiplier λ respectively.

The weak form can therefore be stated as finding $(\mathbf{u}, p, \lambda) \in \mathscr{V}_u \times \mathscr{V}_p \times \mathscr{V}_\lambda$ such that there holds:

$$\int_\Omega \left[\nabla\Phi : (\boldsymbol{\sigma}' - p\mathbf{I}_{2\times 2}) + \Phi\cdot\mathbf{b}\right] \mathrm{d}\Omega + \int_{\Gamma_t} (\Phi\cdot\widehat{\mathbf{t}})\, \mathrm{d}\Gamma = 0, \tag{11a}$$

$$\int_\Omega \left[\phi\left(\frac{\partial \varepsilon_v}{\partial t} + n\beta\frac{\partial p}{\partial t}\right) + \frac{k}{\gamma_w}\nabla\phi\cdot\nabla p\right] \mathrm{d}\Omega + \int_{\Gamma_v} (\phi\widehat{v}_w^n)\, \mathrm{d}\Gamma + \int_{\Omega_L} (\phi\lambda)\, \mathrm{d}\Omega = 0, \tag{11b}$$

$$\int_{\Omega_L} \left[w(p - P_b - \gamma' z)\right] \mathrm{d}\Omega = 0, \tag{11c}$$

for all $(\Phi, \phi, w) \in \mathscr{V}_\Phi \times \mathscr{V}_\phi \times \mathscr{V}_w$.

Eq. (11c) is the weak form of the constraint Eq. (9). Eq. (9) further introduces another additional variational term $\int_{\Omega_L}(\phi\lambda)\,\mathrm{d}\Omega$ (the last term in Eq. (11b)) into the weak form. The introduced term $\int_{\Omega_L}(\phi\lambda)\,\mathrm{d}\Omega$ represents the virtual work in the liquefied zone contributed by the Lagrange multiplier λ. If we compare the term $\int_{\Omega_L}(\phi\lambda)\,\mathrm{d}\Omega$ with the first term in Eq. (11b), i.e. $\int_\Omega \left[\phi\left(\frac{\partial \varepsilon_v}{\partial t} + n\beta\frac{\partial p}{\partial t}\right)\right] \mathrm{d}\Omega$, the physical meaning of the Lagrange multiplier can be clarified as the volume change per unit time per unit volume. If we compare $\int_{\Omega_L}(\phi\lambda)\,\mathrm{d}\Omega$ with the term $\int_{\Gamma_v}(\phi\widehat{v}_w^n)\,\mathrm{d}\Gamma$ in Eq. (11b), the physical meaning of the Lagrange multiplier can be clarified as the pore-fluid flux per unit volume. If we regard $\int_{\Omega_L}(\phi\lambda)\,\mathrm{d}\Omega$ simply as a source term added into the equation, the Lagrange multiplier can be also clarified as a fictitious pore-fluid flux per unit volume, which has a unit of $1/\mathrm{s}$. This issue will be further discussed in Section 4.

3.3. Spatial discretization

For spatial discretization, a standard finite element partitioning of the domain Ω is considered. A trial space $(\mathscr{V}_u)_h \times (\mathscr{V}_p)_h \times (\mathscr{V}_\lambda)_h$ and a weighting space $(\mathscr{V}_\Phi)_h \times (\mathscr{V}_\phi)_h \times (\mathscr{V}_w)_h$ are then introduced as the discrete version of the spaces $\mathscr{V}_u \times \mathscr{V}_p \times \mathscr{V}_\lambda$ and $\mathscr{V}_\Phi \times \mathscr{V}_\phi \times \mathscr{V}_w$, respectively. The subscript h is used hereafter to indicate that the corresponding spaces or quantities are spatially discrete versions. Therefore, the discrete form of Eq. (11) can be written as finding $(\mathbf{u}_h, p_h, \lambda_h) \in (\mathscr{V}_u)_h \times (\mathscr{V}_p)_h \times (\mathscr{V}_\lambda)_h$ such that there holds:

$$\int_\Omega \left[\nabla\Phi_h : (\boldsymbol{\sigma}_h' - p_h\mathbf{I}_{2\times 2}) + \Phi_h\cdot\mathbf{b}\right] \mathrm{d}\Omega + \int_{\Gamma_t} (\Phi_h\cdot\widehat{\mathbf{t}})\, \mathrm{d}\Gamma = 0, \tag{12a}$$

$$\int_\Omega \left\{\phi_h\left[\frac{\partial(\varepsilon_v)_h}{\partial t} + n\beta\frac{\partial p_h}{\partial t}\right] + \frac{k}{\gamma_w}\nabla\phi_h\cdot\nabla p_h\right\} \mathrm{d}\Omega + \int_{\Gamma_v} (\phi_h\widehat{v}_w^n)\, \mathrm{d}\Gamma + \int_{\Omega_L} (\phi_h\lambda_h)\, \mathrm{d}\Omega = 0, \tag{12b}$$

$$\int_{\Omega_L} \left[w_h(p_h - P_b - \gamma' z)\right] \mathrm{d}\Omega = 0, \tag{12c}$$

for all $(\Phi_h, \phi_h, w_h) \in (\mathscr{V}_\Phi)_h \times (\mathscr{V}_\phi)_h \times (\mathscr{V}_w)_h$.

3.4. Temporal discretization

For temporal discretization, the backward Euler method is applied in this work. To keep the resultant matrix system symmetric, a time integration is applied to both Eq. (12b) and Eq. (12c). The fully discrete variational formulation is obtained as follows:

$$\int_\Omega \left[\nabla\Phi_h : (\boldsymbol{\sigma}_h'^t - p_h^t\mathbf{I}_{2\times 2})\right] \mathrm{d}\Omega = -\int_\Omega (\Phi_h\cdot\mathbf{b})\, \mathrm{d}\Omega - \int_{\Gamma_t} (\Phi_h\cdot\widehat{\mathbf{t}})\, \mathrm{d}\Gamma, \tag{13a}$$

$$\int_\Omega \left[\phi_h(\varepsilon_v)_h^t\right] \mathrm{d}\Omega + \int_\Omega \left(\phi_h n\beta p_h^t + \tau\frac{k}{\gamma_w}\nabla\phi_h\cdot\nabla p_h^t\right) \mathrm{d}\Omega + \tau\int_{\Omega_L} (\phi_h\lambda_h^t)\, \mathrm{d}\Omega = \int_\Omega \left[\phi_h(\varepsilon_v)_h^{t-\tau} + \phi_h n\beta p_h^{t-\tau}\right] \mathrm{d}\Omega - \tau\int_{\Gamma_v} (\phi_h\widehat{v}_w^n)\, \mathrm{d}\Gamma, \tag{13b}$$

$$\tau\int_{\Omega_L} (w_h p_h^t)\, \mathrm{d}\Omega = \tau\int_{\Omega_L} \left[w_h(P_b + \gamma' z)\right] \mathrm{d}\Omega, \tag{13c}$$

where τ denotes the time step.

3.5. Matrix representation

In the present model, $\mathbf{d}_u, \mathbf{d}_p$ and $\mathbf{d}_\lambda$ are used to denote the discrete unknown vectors for the displacement (u), the excessive pore pressure (p) and the Lagrange multiplier (λ). Their shape function matrices are denoted by $\mathbf{N}_u, \mathbf{N}_p$ and $\mathbf{N}_\lambda$, respectively. Within the use of the standard Galerkin method, $\mathbf{N}_u, \mathbf{N}_p$ and $\mathbf{N}_\lambda$ are also the weighting function vectors. Eq. (13) can then be rewritten as the following matrix system:

$$\begin{bmatrix} \mathbf{K} & \mathbf{G} & \mathbf{0} \\ \mathbf{G}^{\mathrm{T}} & \mathbf{H} & \mathbf{M} \\ \mathbf{0} & \mathbf{M}^{\mathrm{T}} & \boldsymbol{\delta} \end{bmatrix} \begin{Bmatrix} \mathbf{d}_u \\ \mathbf{d}_p \\ \mathbf{d}_\lambda \end{Bmatrix} = \begin{Bmatrix} \mathbf{F}_u \\ \mathbf{F}_p \\ \mathbf{F}_\lambda \end{Bmatrix}, \tag{14}$$

where

$$\begin{aligned} \mathbf{K} &= \int_\Omega (\mathbf{B}^{\mathrm{T}}\mathbf{D}\mathbf{B})\, \mathrm{d}\Omega, \quad \mathbf{G} = -\int_\Omega (\mathbf{B}^{\mathrm{T}}\mathbf{m}\mathbf{N}_p)\, \mathrm{d}\Omega, \quad \mathbf{B} = \nabla\mathbf{N}_u, \\ \mathbf{H} &= -\int_\Omega \left(n\beta\mathbf{N}_p^{\mathrm{T}}\mathbf{N}_p\right) \mathrm{d}\Omega - \tau\int_\Omega \left[\frac{k}{\gamma_w}(\nabla\mathbf{N}_p)^{\mathrm{T}}\nabla\mathbf{N}_p\right] \mathrm{d}\Omega, \\ \mathbf{F}_u &= -\int_\Omega (\mathbf{N}_u^{\mathrm{T}}\mathbf{b})\, \mathrm{d}\Omega - \int_{\Gamma_t} (\mathbf{N}_u^{\mathrm{T}}\widehat{\mathbf{t}})\, \mathrm{d}\Gamma, \\ \mathbf{F}_p &= \mathbf{G}^{\mathrm{T}}\mathbf{d}_u^{t-\tau} - \left[\int_\Omega \left(n\beta\mathbf{N}_p^{\mathrm{T}}\mathbf{N}_p\right) \mathrm{d}\Omega\right]\mathbf{d}_p^{t-\tau} + \tau\int_{\Gamma_v} \left(\mathbf{N}_p^{\mathrm{T}}\widehat{v}_w^n\right) \mathrm{d}\Gamma, \end{aligned} \tag{15}$$

with $\mathbf{m}$ denoting a vector equivalent to Kronecker Delta tensor. $\mathbf{M}, \boldsymbol{\delta}$ and $\mathbf{F}_\lambda$ in Eq. (14) are associated with the liquefied and non-liquefied zones,

thus are split into sub blocks as below.

Let $\mathscr{L}$ and $\mathscr{N}$ be the subsets of nodes in liquefied and non-liquefied zones, respectively. $\mathscr{L}$ and $\mathscr{N}$ fulfill the following relation:

$$\mathscr{L} \cap \mathscr{N} = \emptyset, \quad \mathscr{L} \cup \mathscr{N} = \mathscr{W}, \tag{16}$$

where $\mathscr{W}$ denotes the set of all the finite element nodes. Eq. (14) is then rewritten as the following sub-block form:

$$\begin{bmatrix} \mathbf{K} & \mathbf{G}^{\mathscr{W}\mathscr{N}} & \mathbf{G}^{\mathscr{W}\mathscr{L}} & \mathbf{0} & \mathbf{0} \\ \mathbf{G}^{\mathscr{N}\mathscr{W}} & \mathbf{H}^{\mathscr{N}\mathscr{N}} & \mathbf{H}^{\mathscr{N}\mathscr{L}} & \mathbf{0} & \mathbf{0} \\ \mathbf{G}^{\mathscr{L}\mathscr{W}} & \mathbf{H}^{\mathscr{L}\mathscr{N}} & \mathbf{H}^{\mathscr{L}\mathscr{L}} & \mathbf{0} & \mathbf{C} \\ \mathbf{0} & \mathbf{0} & \mathbf{0} & \mathbf{I}^{\mathscr{N}\mathscr{N}} & \mathbf{0} \\ \mathbf{0} & \mathbf{0} & \mathbf{C}^{\mathrm{T}} & \mathbf{0} & \mathbf{0} \end{bmatrix} \begin{Bmatrix} \mathbf{d}_u \\ \mathbf{d}_p^{\mathscr{N}} \\ \mathbf{d}_p^{\mathscr{L}} \\ \mathbf{d}_\lambda^{\mathscr{N}} \\ \mathbf{d}_\lambda^{\mathscr{L}} \end{Bmatrix} = \begin{Bmatrix} \mathbf{F}_u \\ \mathbf{F}_p^{\mathscr{N}} \\ \mathbf{F}_p^{\mathscr{L}} \\ \mathbf{0} \\ \mathbf{F}_\lambda^{\mathscr{L}} \end{Bmatrix}, \tag{17}$$

where $\mathbf{I}^{\mathscr{N}\mathscr{N}}$ is a $n_{NL} \times n_{NL}$ identity matrix, with n_{NL} denoting the number of non-liquefied nodes. The matrix $\mathbf{C}$ and the vector $\mathbf{F}_\lambda^{\mathscr{L}}$ are as follows:

$$\mathbf{C} = -\tau \int_{\Omega_L} \left(\mathbf{N}_p^{\mathrm{T}} \mathbf{N}_\lambda\right) \mathrm{d}\Omega, \ \mathbf{F}_\lambda^{\mathscr{L}} = -\tau \int_{\Omega_L} \left[\mathbf{N}_\lambda^{\mathrm{T}} (P_b + \gamma' z)\right] \mathrm{d}\Omega, \tag{18}$$

Now we obtain the following sub-block forms of $\mathbf{M}, \boldsymbol{\delta}$ and $\mathbf{F}_\lambda$:

$$\mathbf{M} = \begin{bmatrix} \mathbf{0} & \mathbf{0} \\ \mathbf{0} & \mathbf{C} \end{bmatrix}, \ \boldsymbol{\delta} = \begin{bmatrix} \mathbf{I}^{\mathscr{N}\mathscr{N}} & \mathbf{0} \\ \mathbf{0} & \mathbf{0} \end{bmatrix}, \ \mathbf{F}_\lambda = \begin{Bmatrix} \mathbf{0} \\ \mathbf{F}_\lambda^{\mathscr{L}} \end{Bmatrix}. \tag{19}$$

3.6. The discrete multiplier space

It can be found that the integral terms $\mathbf{C}$ and $\mathbf{F}_\lambda^{\mathscr{L}}$ in Eq. (18) can only be computed after the interface between liquefied and non-liquefied zones is traced. However, tracing the interface Γ_L shown in Fig. 4 (or called as the liquefaction boundary hereafter) should address the following two issues.

First, the interface Γ_L will be across the elements. This issue is similar to the crack analysis by using the extended finite element method (Belytschko and Black, 1999; Moës et al., 1999; Tian et al., 2019) wherein the cut-cell quadrature and the level set method is used. In this paper, we use a naive choice of the discrete multiplier space to minimize the implementation effort, i.e. the Direct delta function is applied to interpolate the multipliers. In the other words, the pointwise strong form of Eq. (9) is applied. With this simplification, the cut-cell quadrature is avoided and the liquefaction state is determined at each finite element nodes. However, the simplified treatment poses consequences in leading to a non-smooth interface Γ_L, as to be demonstrated in Sections 5 and 6. Nevertheless, the choice here makes the numerical implementation convenient. Furthermore, the multipliers can be statically condensed to improve the computational efficiency, as presented below.

By using the pointwise strong form of the constraint by Eq. (9), $\mathbf{C}$ and

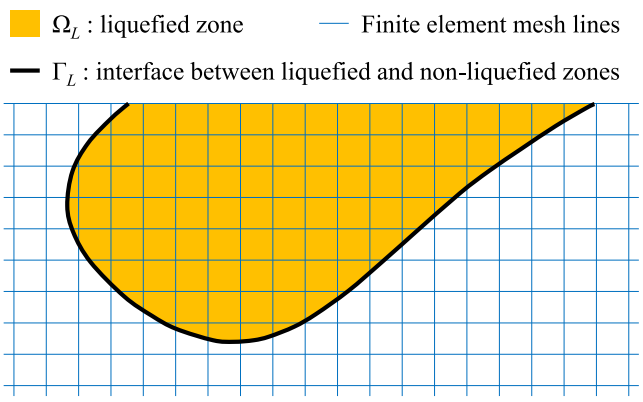

Fig. 4. Schematic of the interface between liquefied and non-liquefied zones.

$\mathbf{F}_\lambda^{\mathscr{L}}$ in Eq. (18) are simplified as the following:

$$\mathbf{C} = -\tau \mathbf{I}^{\mathscr{L}\mathscr{L}}, \ \mathbf{F}_\lambda^{\mathscr{L}} = -\tau \left(\mathbf{P}_b^{\mathscr{L}} + \gamma' \mathbf{z}^{\mathscr{L}}\right), \tag{20}$$

where $\mathbf{I}^{\mathscr{L}\mathscr{L}}$ is a $n_L \times n_L$ identity matrix, with n_L denoting the number of liquefied nodes. $\mathbf{P}_b^{\mathscr{L}}$ is a vector collecting the values of P_b at all liquefied nodes. $\mathbf{z}^{\mathscr{L}}$ is a vector collecting the values of z at all liquefied nodes. Noting the diagonal property of the matrix $\mathbf{C}$, the third and fourth rows of Eq. (17) gives the following condensation of the Lagrange multipliers:

$$\mathbf{d}_\lambda^{\mathscr{L}} = \frac{1}{\tau}\left(\mathbf{G}^{\mathscr{L}\mathscr{W}} \mathbf{d}_u + \mathbf{H}^{\mathscr{L}\mathscr{N}} \mathbf{d}_p^{\mathscr{N}} + \mathbf{H}^{\mathscr{L}\mathscr{L}} \mathbf{d}_p^{\mathscr{L}} - \mathbf{F}_p^{\mathscr{L}}\right), \quad \mathbf{d}_\lambda^{\mathscr{N}} = 0. \tag{21}$$

This means that the Lagrange multipliers are no longer the unknowns in the matrix system, making Eq. (17) condensed as follows:

$$\begin{bmatrix} \mathbf{K} & \mathbf{G}^{\mathscr{W}\mathscr{N}} & \mathbf{G}^{\mathscr{W}\mathscr{L}} \\ \mathbf{G}^{\mathscr{N}\mathscr{W}} & \mathbf{H}^{\mathscr{N}\mathscr{N}} & \mathbf{H}^{\mathscr{N}\mathscr{L}} \\ \mathbf{0} & \mathbf{0} & \mathbf{I}^{\mathscr{L}\mathscr{L}} \end{bmatrix} \begin{Bmatrix} \mathbf{d}_u \\ \mathbf{d}_p^{\mathscr{N}} \\ \mathbf{d}_p^{\mathscr{L}} \end{Bmatrix} = \begin{Bmatrix} \mathbf{F}_u \\ \mathbf{F}_p^{\mathscr{N}} \\ \mathbf{P}_b^{\mathscr{L}} + \gamma' \mathbf{z}^{\mathscr{L}} \end{Bmatrix}. \tag{22}$$

The third row of Eq. (22), i.e. $\mathbf{d}_p^{\mathscr{L}} = \mathbf{P}_b^{\mathscr{L}} + \gamma' \mathbf{z}^{\mathscr{L}}$, can then be inserted into the first and second rows:

$$\begin{bmatrix} \mathbf{K} & \mathbf{G}^{\mathscr{W}\mathscr{N}} & \mathbf{0} \\ \mathbf{G}^{\mathscr{N}\mathscr{W}} & \mathbf{H}^{\mathscr{N}\mathscr{N}} & \mathbf{0} \\ \mathbf{0} & \mathbf{0} & \mathbf{I}^{\mathscr{L}\mathscr{L}} \end{bmatrix} \begin{Bmatrix} \mathbf{d}_u \\ \mathbf{d}_p^{\mathscr{N}} \\ \mathbf{d}_p^{\mathscr{L}} \end{Bmatrix} = \begin{Bmatrix} \mathbf{F}_u - \mathbf{G}^{\mathscr{W}\mathscr{L}}\left(\mathbf{P}_b^{\mathscr{L}} + \gamma' \mathbf{z}^{\mathscr{L}}\right) \\ \mathbf{F}_p^{\mathscr{N}} - \mathbf{H}^{\mathscr{N}\mathscr{L}}\left(\mathbf{P}_b^{\mathscr{L}} + \gamma' \mathbf{z}^{\mathscr{L}}\right) \\ \mathbf{P}_b^{\mathscr{L}} + \gamma' \mathbf{z}^{\mathscr{L}} \end{Bmatrix}. \tag{23}$$

The third row and the third column of Eq. (23) can be further eliminated:

$$\begin{bmatrix} \mathbf{K} & \mathbf{G}^{\mathscr{W}\mathscr{N}} \\ \mathbf{G}^{\mathscr{N}\mathscr{W}} & \mathbf{H}^{\mathscr{N}\mathscr{N}} \end{bmatrix} \begin{Bmatrix} \mathbf{d}_u \\ \mathbf{d}_p^{\mathscr{N}} \end{Bmatrix} = \begin{Bmatrix} \mathbf{F}_u - \mathbf{G}^{\mathscr{W}\mathscr{L}}\left(\mathbf{P}_b^{\mathscr{L}} + \gamma' \mathbf{z}^{\mathscr{L}}\right) \\ \mathbf{F}_p^{\mathscr{N}} - \mathbf{H}^{\mathscr{N}\mathscr{L}}\left(\mathbf{P}_b^{\mathscr{L}} + \gamma' \mathbf{z}^{\mathscr{L}}\right) \end{Bmatrix}. \tag{24}$$

Eq. (24) avoids the well-known saddle-point difficulty caused by Eq. (17). Meanwhile, the system size of Eq. (24) is smaller than Eq. (17). Therefore, the computational efficiency is guaranteed.

The remaining issue is that the liquefied zone (Ω_L) is undetermined and time-dependent. Typically, a trial-and-error procedure can be applied to iteratively solve this type of problem. During the first iteration, we can start from the conventional numerical model with constant permeability and the liquefaction criterion by Eq. (7), so as to provide an initial guess of Ω_L. The second iteration would impose the pore pressure constraints by Eq. (9), i.e. $(p - P_b - \gamma' z = 0)$ in Ω_L. Then, subsequent iterative corrections are required until converging to a solution satisfying given conditions. However, the problem is that we still have no such given conditions to iteratively correct Ω_L. This will lead to a consequence that the iterative procedure would finish in only two iterations. The solution would give an identical Ω_L to the initial guess, and meanwhile the tensile behavior is removed. This result would disagree with the previous numerical investigations (Zhou et al., 2020b) wherein eliminating the tensile behavior has significant influences on Ω_L. That is, the hydro-mechanical response influences the liquefied zone Ω_L which in turn influences the hydro-mechanical response. Therefore, we still need to find a complementarity condition which can be used to check whether the current liquefied zone (Ω_L) is physically reasonable or not. This issue is addressed in Section 4 by finding the dual condition, so as to model the physical problem of seabed liquefaction as a nonlinear complementarity problem in a mathematical manner.

4. The nonlinear complementarity problem

If we recall Eq. (11b), the physical meaning of the Lagrange multiplier λ can be interpreted as a source term added into the origin governing equations. In Section 3, with the discretization and the use of pointwise strong-from constraint, Eq. (11b) becomes Eq. (21). Therefore, we can further distinguish from Eq. (21) that the Lagrange

multiplier λ has the unit of m^3/s, representing a fictitious pore-fluid flux, or the volume change of the soil column per unit time.

To remove the tensile behavior in the liquefied zone, the additional source term is needed to help the excessive pore pressure decreasing in an appropriate way such that the vertical effective stress $\bar{\sigma}_v'$ equals to zero in the liquefied zone. This requirement calls for that the source term λ should not be negative. Therefore, the following dual condition is obtained:

$$\lambda \geqslant 0 \quad \text{in} \quad \Omega_L, \quad \lambda = 0 \quad \text{in} \quad \Omega_{NL}. \tag{25}$$

Taking into account the primal condition by Eq. (9) proposed in Section 3.1, we now obtain the following KKT condition in terms of primal and dual variables:

$$[p - P_b - \gamma' z \leqslant 0, \quad \lambda \geqslant 0, \quad (p - P_b - \gamma' z)\lambda = 0] \quad \text{in} \quad \Omega. \tag{26}$$

Noting that the pointwise strong form of the constraint is applied in this work, the discrete KKT condition is simplified as follows:

$$\left[\mathbf{d}_p\right]_i - \left[\mathbf{P}_b\right]_i - \gamma' \left[\mathbf{z}\right]_i \leqslant 0, \quad \left[\mathbf{d}_\lambda\right]_i \geqslant 0, \quad \left\{\left[\mathbf{d}_p\right]_i - \left[\mathbf{P}_b\right]_i - \gamma' \left[\mathbf{z}\right]_i\right\}\left[\mathbf{d}_\lambda\right]_i = 0, \tag{27}$$

where $\mathbf{P}_b$ and $\mathbf{z}$ are vectors collecting the values of P_b and z at all nodes, respectively. The subscript i denotes that the corresponding variables are defined at the node i.

To solve the NCP numerically, the primal–dual active set strategy (Kunisch and RöSch, 2002) is applied. First, we rewrite the discrete KKT condition by the two subsets $\mathscr{L}$ and $\mathscr{N}$:

$$\begin{aligned} \left[\mathbf{d}_p^{\mathscr{L}}\right]_i &= \left[\mathbf{P}_b^{\mathscr{L}}\right]_i + \gamma' \left[\mathbf{z}^{\mathscr{L}}\right]_i, \quad \left[\mathbf{d}_\lambda^{\mathscr{L}}\right]_i \geqslant 0 \quad \text{in} \quad \Omega_L, \\ \left[\mathbf{d}_p^{\mathscr{N}}\right]_i &< \left[\mathbf{P}_b^{\mathscr{N}}\right]_i + \gamma' \left[\mathbf{z}^{\mathscr{N}}\right]_i, \quad \left[\mathbf{d}_\lambda^{\mathscr{N}}\right]_i = 0 \quad \text{in} \quad \Omega_{NL}, \end{aligned} \tag{28}$$

where $\mathbf{P}_b^{\mathscr{N}}$ and $\mathbf{z}^{\mathscr{N}}$ are vectors composed of P_b and z at non-liquefied nodes, respectively.

Then, the iterative procedure is summarized as follows:

(1) Guess the current subsets $\mathscr{L}$ and $\mathscr{N}$ of liquefied nodes. For the initial case (i.e. the 1st iteration in the 1st time step), $\mathscr{L}$ is assumed to be empty. For other cases, $\mathscr{L}$ and $\mathscr{N}$ are assumed as the historical subsets.
(2) Assemble the matrices $\mathbf{K}$, $\mathbf{G}$ and $\mathbf{H}$; compute the vectors $\mathbf{F}$, $\mathbf{P}_b$ and $\mathbf{z}$.
(3) Solve the linear system by Eq. (24).
(4) Update the displacement $\mathbf{d}_u$ and the pore pressure $\mathbf{d}_p^{\mathscr{N}}$.
(5) Set the pore pressure for liquefied nodes according to the pointwise strong form of the constraint by Eq. (9): $\mathbf{d}_p^{\mathscr{L}} = \mathbf{P}_b^{\mathscr{L}} + \gamma' \mathbf{z}^{\mathscr{L}}$.
(6) Calculate the multipliers by Eq. (21).
(7) Update the subsets $\mathscr{L}$ and $\mathscr{N}$. For the current subset $\mathscr{L}$, those nodes not fulfilling $\left[\mathbf{d}_\lambda^{\mathscr{L}}\right]_i \geqslant 0$ are moved from $\mathscr{L}$ to $\mathscr{N}$. For the current subset $\mathscr{N}$, those nodes not fulfilling $\left[\mathbf{d}_p^{\mathscr{N}}\right]_i < \left[\mathbf{P}_b^{\mathscr{N}}\right]_i + \gamma' \left[\mathbf{z}^{\mathscr{N}}\right]_i$ are moved from $\mathscr{N}$ to $\mathscr{L}$.
(8) If $\epsilon_u < \hat{\epsilon}_u$ and $\epsilon_p < \hat{\epsilon}_p$, go to next time step; otherwise, go back to step 1. $\hat{\epsilon}_u$ and $\hat{\epsilon}_p$ are two pre-defined convergence tolerances. In this work, $\hat{\epsilon}_u = \hat{\epsilon}_p = 1 \times 10^{-6}$ is applied. ϵ_u and ϵ_p are two residuals defined as follows:

$$\epsilon_u = \|\Delta \mathbf{d}_u\|_2 / (\mathbf{d}_u), \quad \epsilon_p = \|\Delta \mathbf{d}_p\|_2 / (\mathbf{d}_p), \tag{29}$$

where $\|\Delta \mathbf{d}_u\|_2$ and $\|\Delta \mathbf{d}_p\|_2$ are the L^2-norms of the incremental solution for displacement and pore pressure, respectively. $\|\mathbf{d}_u\|_2$ and $\|\mathbf{d}_p\|_2$ are the L^2-norms of the total solution.

The above procedure is implemented in the in-house finite element code (Zhou et al., 2018; Wang et al., 2019; Zhou et al., 2020a; Zhou et al., 2020b), which will be validated by analytical solutions with constant permeability in the next two sections.

5. Cylinder tests under one-dimensional (1D) wave loading

In this section, the cylinder tests (Liu et al., 2015) are simulated by three numerical treatments, i.e., CP (the conventional Darcy model using **Constant Permeability**), DP (**Dynamic Permeability** model by Zhou et al. (2020b)) and NCP (the present model). The DP model (Zhou et al., 2020b) is given as follows:

$$k_d = \begin{cases} k, & \text{if } r_u \leqslant r_u^{\text{cr}} \\ \left[1 + (c_1 - 1)\left(r_u - r_u^{\text{cr}}\right)^{c_2}\right]k, & \text{if } r_u > r_u^{\text{cr}} \end{cases}. \tag{30}$$

where k_d is the dynamic permeability and k denotes the initial value. r_u is the excess pore pressure ratio given by: $r_u = (p - P_b)/(\gamma' z)$. c_1, c_2 and r_u^{cr} are model parameters. As discussed in Zhou et al. (2020b), the parameters $c_1 = 100, c_2 = 1$ and $r_u^{\text{cr}} = 1$ are recommended. Therefore, this group of parameters is applied in this section when using the DP model. It is notable that NCP is a parameter-free treatment.

The boundary conditions are shown in Fig. 5, where the only difference from Fig. 1 is that the wave loading conditions are 1D here. This means that the wave pressure P_b is still determined by Eq. (4a) but $x = 0$ is applied. The element sizes along the x and z directions are taken as 1 m and 0.12 m, respectively. For the temporal discretization, one wave

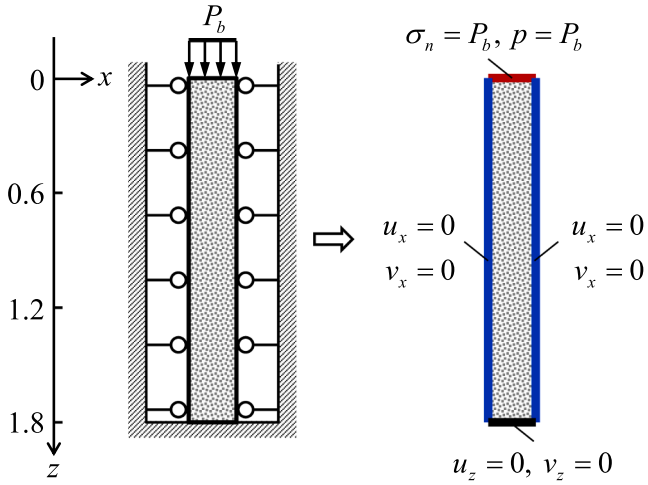

Fig. 5. Boundary conditions of the cylinder tests.

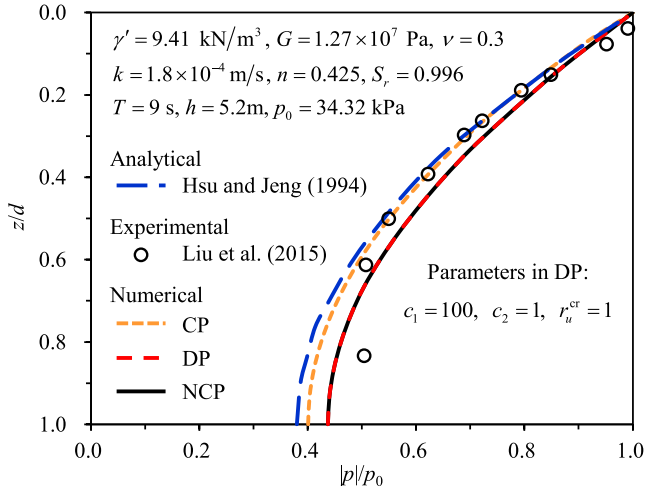

Fig. 6. The pressure amplitude $|p|/p_0$ versus the soil depth z/d in 'Test 20'.

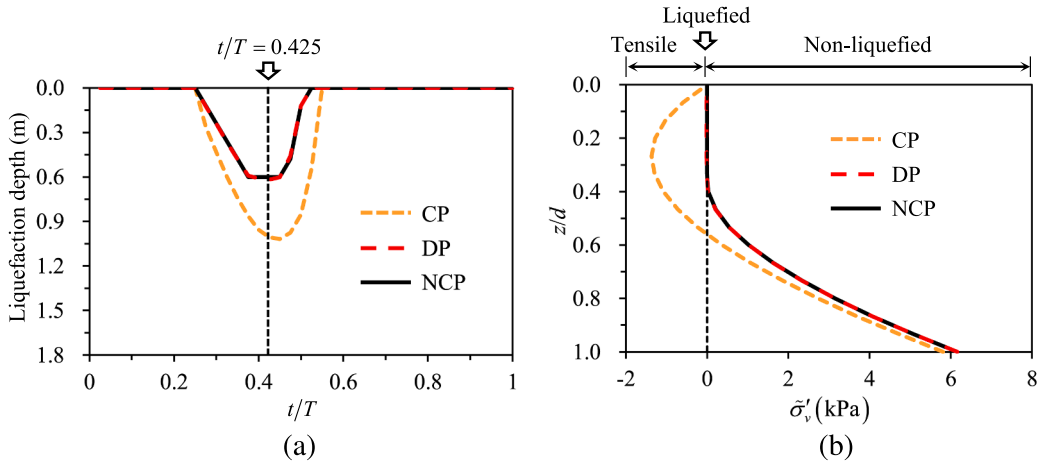

Fig. 7. Numerical results of 'Test 20': (a) temporal liquefaction depth; and (b) vertical distribution of $\tilde{\sigma}_v'$ at $t = 0.425T$.

period T is divided into 40 time steps, i.e. the time step τ is taken as $0.025T$.

5.1. Pore pressure and liquefaction analysis

First, the 'Test 20', see Table 2 in Liu et al. (2015), is simulated. According to experimental results (Liu et al., 2015), liquefaction was observed in 'Test 20'. Fig. 6 presents the variation of the pressure amplitude along with the soil depth. The computational parameters are also given in Fig. 6, where G is the shear modulus and ν is the Poisson's ratio.

The analytical solution by Hsu and Jeng (1994) has been widely applied by the ocean engineering community to inspect the numerical performances. As shown in Fig. 6, there is a slight deviation between the CP model and the analytical solution (Hsu and Jeng, 1994). Nevertheless, similar deviations were also reported in other works (Sumer and Fredsøe, 2002; Chen et al., 2019; Duan et al., 2019; Chen et al., 2020) and the comparison here is therefore capable of validating the numerical code developed in this paper.

Fig. 6 also indicates that the DP model and the the present model (NCP) obtain nearly identical results and they both coincide with the experimental data in a reasonable sense. As compared with the CP model, DP and NCP both result in a decrease in the pressure amplitude, but the decrease is not significant. Note that the comparison in Fig. 6 cannot be regarded as that DP and NCP has negligible influences on the numerical results, because only the pressure amplitude is compared in Fig. 6. If other results (e.g., the vertical effective stress) are compared, the differences can become apparent, as presented in Fig. 7.

Fig. 7(a) provides the liquefaction depth determined by the liquefaction criterion Eq. (7). The liquefaction depths by DP and NCP are nearly identical and apparently smaller than that by CP. It was found by taking a close look into the output data that the tensile behavior caused by CP at the instant of $t = 0.425T$ is the most apparent among all the time steps. Therefore, we take this instant for an instance to investigate in detail the vertical effective stress $\gamma' z - (p - P_b)$, which is represented by $\tilde{\sigma}_v'$ in this work. As shown in Fig. 7(a) and Table 1, the negative values of $\tilde{\sigma}_v'$ are considerable in CP and the maximum tensile stress is −1367.3 Pa. Obviously, tensile behavior does not exist in a non-cohesive seabed (Qi and Gao, 2018). This unphysical behavior is greatly eased by using the DP model wherein the maximum tensile stress is reduced to −12.6 Pa. In contrast, the tensile behavior is totally removed by the present model, wherein $\tilde{\sigma}_v'$ equals exactly to zero in the liquefied zone.

For the DP model, Table 1 also gives the excess pore pressure ratio $r_u = (p - P_b)/(\gamma' z)$ and the ratio of dynamic permeability k to its initial value k_0. For the present model with the NCP treatment, Table 1 further gives the specific values of the Lagrange multiplier λ. These variables are then plotted together in Fig. 8. In Fig. 8(a), we have ($r_u \geqslant 1$, $k/k_0 \geqslant 1$) in

Table 1
Variables at $t = 0.425T$ during the numerical simulation of 'Test 20'.

z (m)	z/d	CP	DP			NCP	
		$\tilde{\sigma}_v'$ (Pa)	$\tilde{\sigma}_v'$ (Pa)	r_u	k/k_0	$\tilde{\sigma}_v'$ (Pa)	$\lambda(10^{-5}\mathrm{m}^3/\mathrm{s})$
0	0	0	0	-	-	0	-
0.12	0.07	−596.5	−7.9	1.007	1.695	0	0.630
0.24	0.13	−1023.0	−10.7	1.005	1.471	0	0.630
0.36	0.20	−1278.5	-12.6	1.004	1.368	0	0.630
0.48	0.27	-1367.3	−8.9	1.002	1.194	0	0.630
0.60	0.33	−1296.8	−4.0	1.001	1.070	0	0.531
0.72	0.40	−1076.8	21.8	0.997	1	25.0	0
0.84	0.47	−718.8	206.9	0.974	1	209.4	0
0.96	0.53	−234.6	542.7	0.940	1	544.7	0
1.08	0.60	363.8	1017.7	0.900	1	1019.3	0
1.20	0.67	1065.2	1619.6	0.857	1	1620.8	0
1.32	0.73	1859.4	2336.1	0.812	1	2337.1	0
1.44	0.80	2737.6	3156.5	0.767	1	3157.4	0
1.56	0.87	3692.5	4071.8	0.722	1	4072.5	0
1.68	0.93	4719.1	5075.1	0.679	1	5075.8	0
1.80	1.00	5814.1	6162.5	0.636	1	6163.2	0
Liquefaction depth (m)		1.007	0.618			0.600	

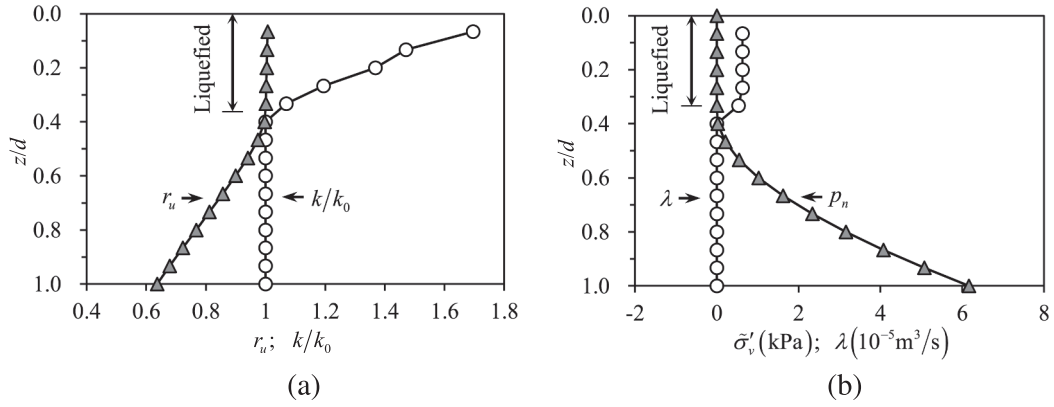

Fig. 8. Vertical distributions of characteristic variables in 'Test 20': (a) r_u and k/k_0 in the DP model; and (b) $\tilde{\sigma}_v'$ and λ in the present model (NCP treatment).

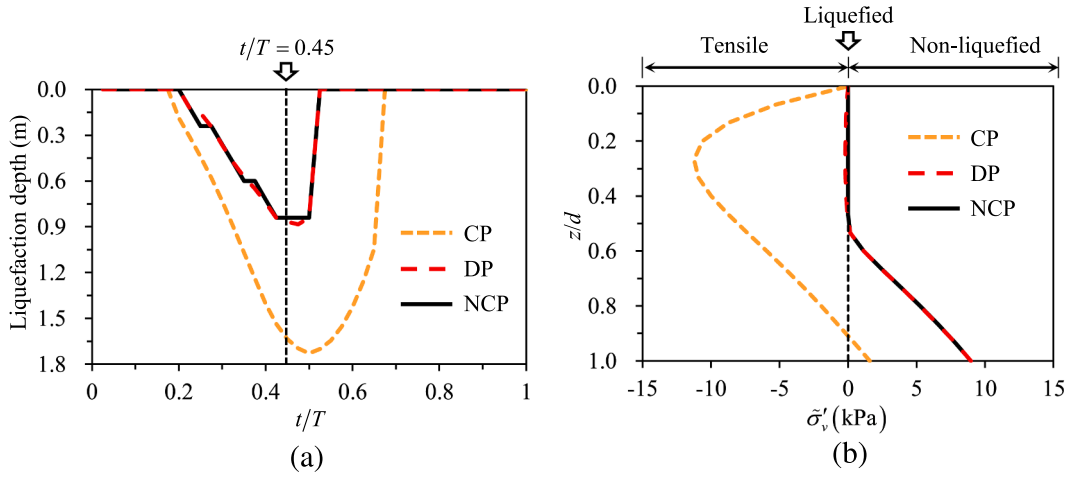

Fig. 9. Numerical results of 'Test 2': (a) temporal liquefaction depth; and (b) vertical distribution of $\tilde{\sigma}_v'$ at $t = 0.45T$.

the liquefied zone and $(r_u < 1,\ k/k_0 = 1)$ in the non-liquefied zone, noting that $r_u = 1$ is approximately fulfilled in the liquefied zone by DP in a 'penalty-like' way. In Fig. 8(b), we have $(\tilde{\sigma}_v' = 0,\ \lambda \geqslant 0)$ in the liquefied zone and $(\tilde{\sigma}_v' > 0,\ \lambda = 0)$ in the non-liquefied zone. These primal and dual values strictly fulfill the KKT condition Eq. (26) proposed in this work for instantaneous liquefaction. The numerical results in Fig. 8 indicate that the non-linearities arising from either DP or NCP converged during the iterative procedure. A further comparison between Figs. 8(a) and 8(b) implies that the effect of permeability increase during liquefaction can be also approximately understood as a fictitious source term added into the liquefied zone. This implies that both DP and NCP have the ability of accelerating the pore-fluid flow during liquefaction and therefore coincide with the intuitive physical understandings as well as existing experimental observations.

Table 2
Variables at $t = 0.45T$ during the numerical simulation of 'Test 2'

z (m)	z/d	CP	DP			NCP	
		$\tilde{\sigma}_v'$ (Pa)	$\tilde{\sigma}_v'$ (Pa)	r_u	k/k_0	$\tilde{\sigma}_v'$ (Pa)	$\lambda(10^{-5}\mathrm{m}^3/\mathrm{s})$
0	0	0	0	-	-	0	-
0.12	0.07	−5212.3	−93.9	1.083	9.234	0	5.621
0.24	0.13	−8733.1	−151.4	1.067	7.640	0	5.621
0.36	0.20	−10637.5	−192.8	1.057	6.637	0	5.621
0.48	0.27	-11240.9	-199.5	1.044	5.374	0	5.621
0.60	0.33	−10914.8	−179.6	1.032	4.151	0	5.621
0.72	0.40	−9996.8	−127.3	1.019	2.861	0	5.621
0.84	0.47	−8751.2	−43.5	1.006	1.545	0	4.552
0.96	0.53	−7362.5	150.9	0.983	1	162.6	0
1.08	0.60	−5945.0	1136.6	0.888	1	1145.3	0
1.20	0.67	−4559.4	2463.5	0.782	1	2472.7	0
1.32	0.73	−3230.1	3873.8	0.688	1	3884.1	0
1.44	0.80	−1959.7	5254.2	0.612	1	5265.3	0
1.56	0.87	−740.8	6566.0	0.553	1	6577.5	0
1.68	0.93	436.8	7802.5	0.506	1	7814.2	0
1.80	1.00	1580.9	8966.6	0.470	1	8978.2	0
Liquefaction depth (m)		1.635		0.867			0.840

The above discussion is based on the simulation of 'Test 20' wherein the degree of saturation S_r is 0.996. As reported in the literature (Jeng, 2018), soil saturation plays an important role in the estimation of wave-seabed interactions. In marine environment, the degree of saturation generally varies from 0.95 to 1.0 (Michallet et al., 2009). Therefore, we simulated another case under a lower saturation ($S_r = 0.951$), i.e. 'Test 2' in Liu et al. (2015). The only difference between 'Test 2' and 'Test 20' is the saturation; other parameters are the same in both tests.

Fig. 9(a) shows the liquefaction depths by three numerical treatments of 'Test 2'. As discussed in Fig. 7(a) for 'Test 20', removing tensile behavior reduces the determined liquefaction depth. The reduction becomes more significant here for the lower saturation degree in 'Test 2', as shown in Fig. 9(a). It is also found that the temporal evolution of the liquefaction depth by NCP is not as smooth as those by CP and DP. The reason is explained here from the following two aspects. First, tensile stresses occur in both CP and DP models (as can be further investigated in Fig. 9(a) and Table 2), despite that the tensile behavior is eased by DP. Therefore, the critical point where $\widetilde{\sigma}_v^{'} = 0$ can be traced across the element during the post-process procedure. This results in a smooth curve of temporal liquefaction depth at the expense of unphysical tensile behavior. Second, the non-smoothness by NCP is caused by that the KKT condition is imposed in a collocation manner. Improvement can be conducted by using weak-form KKT condition but cut-cell quadrature must be applied. Noting that the implementation effort is nontrivial, this issue will be addressed in our future works. Herein, we focus on the use of pointwise strong-form constraints. As to be discussed in Section 5.2, the non-smoothness can be also eased to some extent by using finer computational meshes. It is concluded that the non-smoothness cannot be attributed to the concept of eliminating tensile behavior or the NCP treatment. The naive choice of the discrete multiplier space is actually the main reason. It is noted that this type of non-smoothness also occurs in 'Test 20' but is not as apparent as that in 'Test 2', because the liquefaction potential is lower in 'Test 20'.

For the instant of $t = 0.45T$ when the CP model leads to most conspicuous tensile behavior among all the time steps, Fig. 9(b) gives the vertical distribution of $\widetilde{\sigma}_v^{'}$ in 'Test 2'. Table 2 lists the detailed values of several variables at this instant. As shown in Fig. 9(b) and Table 2, the tensile stresses are abnormally large in the CP model and reach a maximum value of -11240.9 Pa. This value is greatly reduced by DP to -199.5 Pa, which is the residual error of the DP model by using 'penalty-like' treatment. Noting that the residual value by DP is -12.6 Pa in 'Test 20', we can summarize that lower saturation leads to larger residual. Or in other words, if the same accuracy is required, lower saturation needs larger 'penalty-like' parameters. The explanation is straightforward because lower saturation leads to dealing with larger tensile stresses. However, NCP using the Lagrange multiplier method is totally free of this issue. In both 'Test 20' (Table 1) and 'Test 2' (Table 2), $\widetilde{\sigma}_v^{'}$ equals exactly to zero in the liquefied zone.

For r_u and k/k_0 in the DP model listed in Table 2, Fig. 10(a) provides the vertical distribution curve. Analogously, Fig. 10(b) plots the primal and dual values in the present NCP model. Fig. 10 shows that the nonlinearity has been treated to be converged. A further comparison between Fig. 10 and Fig. 8 indicates that lower saturation calls for larger acceleration of the pore-fluid flow during liquefaction. This requirement turns out to be the larger permeability in DP, and on the other hand, the larger multiplier in NCP. The discussion here implies that DP and NCP may have some interesting relations in physical mechanism. A more interesting phenomenon is that, if we take a closer look at the multiplier values in Tables 1 and 2, the multipliers can be found to stay uniform in the liquefied zone, except for that the points near the liquefaction boundary have relatively small multipliers. We envision that future works may find some physical explanations for this numerical phenomenon.

Liu et al. (2015) reported 24 cylinder tests under 1D wave loading conditions using a 1.8 m thick sandy deposit, by changing the soil porosity n, soil saturation S_r, wave period T and pressure amplitude p_0. Twelve of these tests were simulated by using CP and DP models in Zhou et al. (2020b). According to the above investigations, NCP will obtain nearly identical results with DP when we focus on what engineering concerns, such as the pressure amplitude, the liquefaction depth etc. Therefore, here we only take 6 tests for instances to validate the advantages of NCP over CP. Results for other tests are similar to those reported by Zhou et al. (2020b).

Fig. 11 provides the vertical distributions of pressure amplitude. Two values of S_r and three values of p_0 (i.e., p_1, p_2 and p_3) are considered. The cases 'p_1' in Figs. 11(a) and 11(b) correspond to 'Test 20' and 'Test 2' in Liu et al. (2015), respectively. In Fig. 11(a), the numerical results by CP and NCP both coincide with the experimental data in a reasonable sense. In contrast, CP leads to a dramatic discrepancy with the experimental results in Fig. 11(b). This poor performance is greatly improved by using the NCP treatment, especially the overall experimental tendencies are well reproduced. These results can be explained as below with the combination of Fig. 12.

Fig. 12 shows the vertical distributions of $\widetilde{\sigma}_v^{'}$ at specified instants. The instants are different in different tests. How to select the specified instant is the same as Figs. 7(b) and 9(b), i.e. making the selected instant has maximum tensile stress among all the time steps. For soil with relatively high saturation ($S_r = 0.996$), the tensile stress by CP is under a relatively low magnitude, as shown in Fig. 12(a). Therefore, the differences between CP and NCP are not significant in Figs. 11(a) and 12(a). For the experimental tests under pressure $p_2 = 24.52$ kPa and $p_3 = 12.10$ kPa, the numerical results by CP and NCP even stay almost the same. If the saturation is lower, then the differences between CP and NCP become significant. As shown in Fig. 12(b), the tensile stresses are abnormally large by CP and are eliminated by NCP. This improvement by NCP in

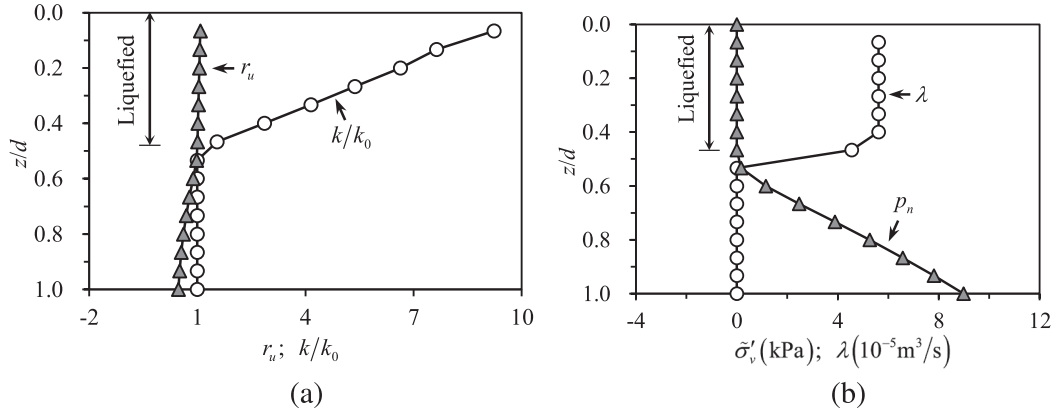

Fig. 10. Vertical distributions of characteristic variables in 'Test 2': (a) r_u and k/k_0 in the DP model; and (b) $\widetilde{\sigma}_v^{'}$ and λ in the present model with the NCP treatment.

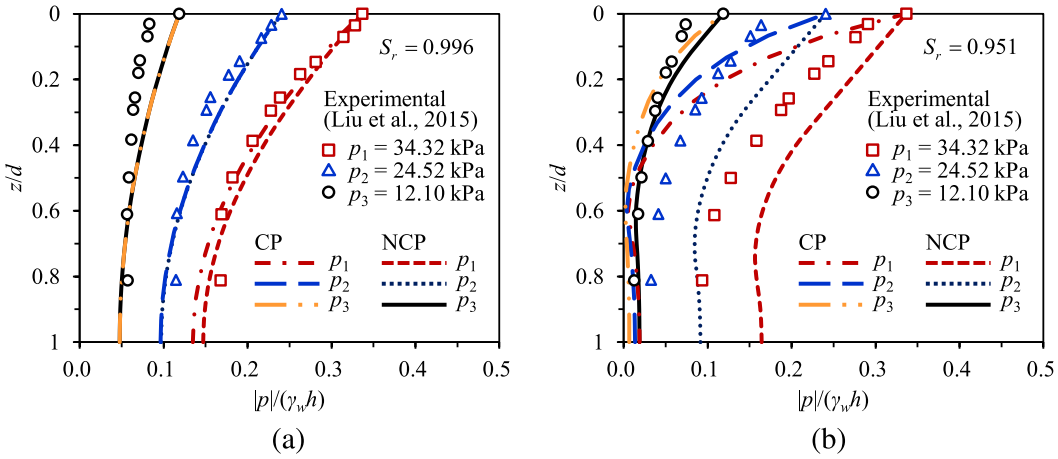

Fig. 11. Vertical distributions of $|p|/(\gamma_w' h)$: (a) $S_r = 0.996$; and (b) $S_r = 0.951$.

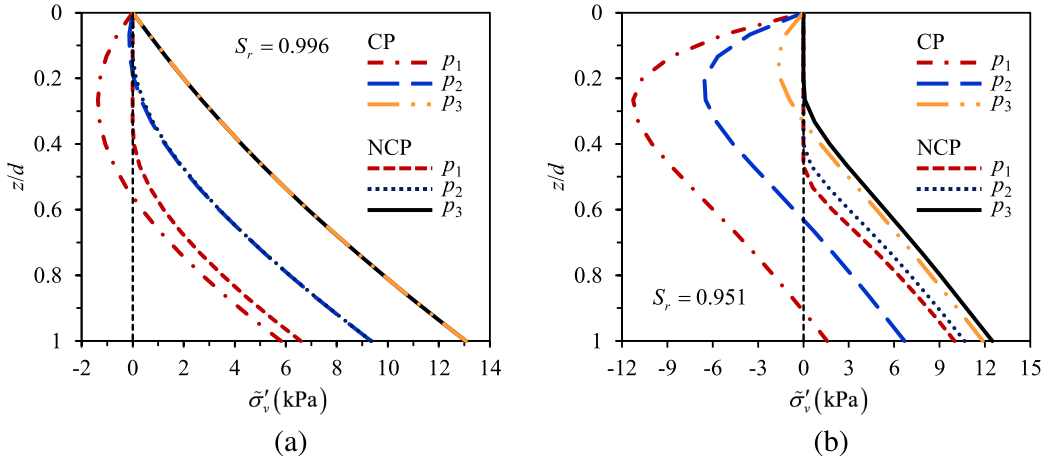

Fig. 12. Vertical distributions of $\tilde{\sigma}_v'$: (a) $S_r = 0.996$; and (b) $S_r = 0.951$.

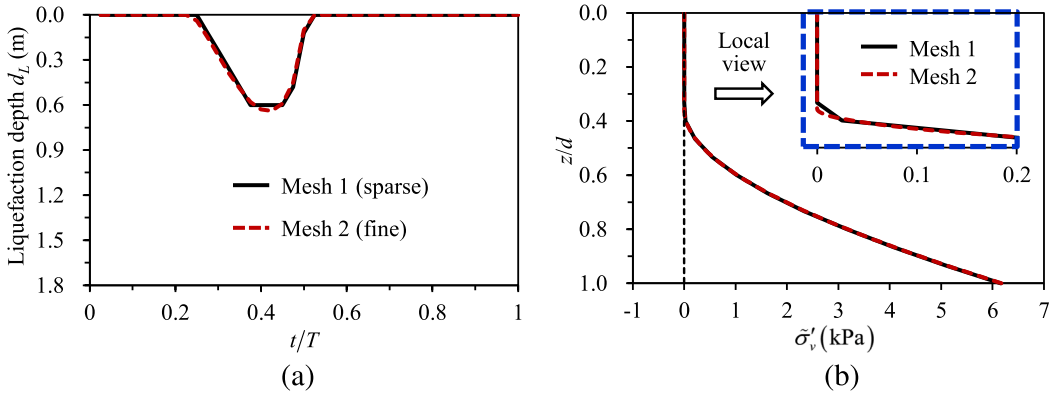

Fig. 13. Numerical results of 'Test 20' using two meshes: (a) temporal liquefaction depth; and (b) vertical distribution of $\tilde{\sigma}_v'$ at $t = 0.425T$.

turn contributes to a better reproduction of the experimental results, as shown in Fig. 11(b).

5.2. *Influence of the mesh density on the liquefaction depth and vertical effective stress*

The above simulation is conducted by using the computational mesh whose element size along the vertical direction is taken as 0.12 m. It is denoted here by 'Mesh 1'. To study the influence of the mesh density, we further conduct several simulations by using a finer mesh ('Mesh 2') whose element size along the vertical direction is 0.01 m. Figs. 13 and 14 are the numerical results of 'Test 20' and 'Test 2', respectively. Figs. 13 (a) and 14(a) show that finer mesh provides smoother temporal distributions of liquefaction depth. This result is not surprising because we impose the KKT condition in a pointwise manner and more points can provide more accurate determination of the liquefaction depth. The

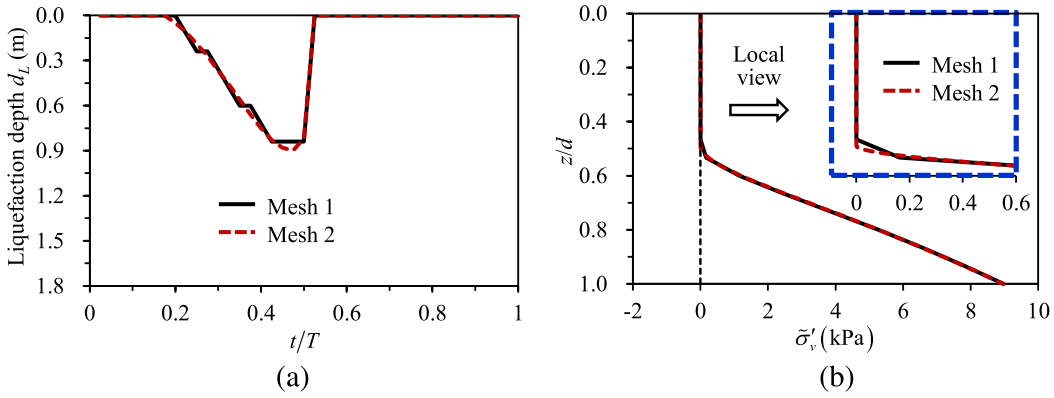

Fig. 14. Numerical results of 'Test 2' using two meshes: (a) temporal liquefaction depth; and (b) vertical distribution of $\tilde{\sigma}'_v$ at $t = 0.45T$.

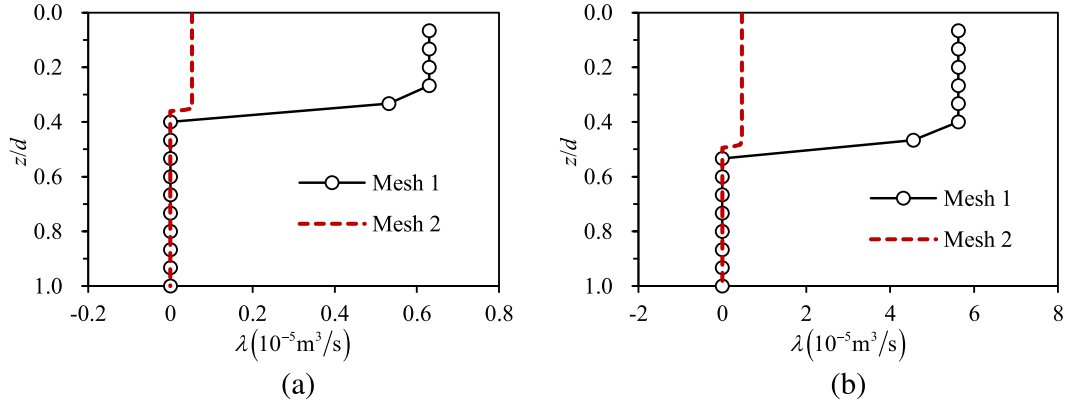

Fig. 15. Vertical distributions of the Lagrange multiplier: (a) 'Test 20' ($S_r = 0.996, t = 0.425T$); and (b) 'Test 2' ($Sr = 0.951, t = 0.45T$).

accuracy of the liquefaction depth is basically the vertical element size. However, the influence of the mesh density on the vertical effective stress is not significant, as shown in Figs. 13(b) and 14(b). The differences can be only observed from the local view in the right upper corner of the figures and are mainly located near the liquefaction boundary. This observation indicates that the additional numerical error by using pointwise KKT condition is not significant from an engineering point of view, and generally we do not need to worry about the accuracy.

If we want to discuss on the numerical error of the NCP treatment in a strict manner, three issues should be addressed. First, we should conduct a mesh convergence study by using a series of meshes. Second, the strong-form KKT condition should be also compared with its weak form. The last issue is to distinguish the numerical error from the former two issues. This strict procedure is difficult in the current work because there still lack numerical treatments of weak-form KKT condition for instantaneous liquefaction as well as NCP-based analytical solutions. The pointwise KKT condition seems somehow sufficient for engineering applications, but it is also of significance to explore the merits of weak-form KKT condition in the future to complete the theoretical discussion.

5.3. *Influence of the mesh density on the Lagrange multiplier*

Fig. 15 shows the vertical distribution of the Lagrange multiplier by two meshes. The results imply that the multiplier stays almost constant in the liquefied zone and finer mesh obtains smaller multiplier. Noting that the two meshes used here are both uniform, if non-uniform mesh is

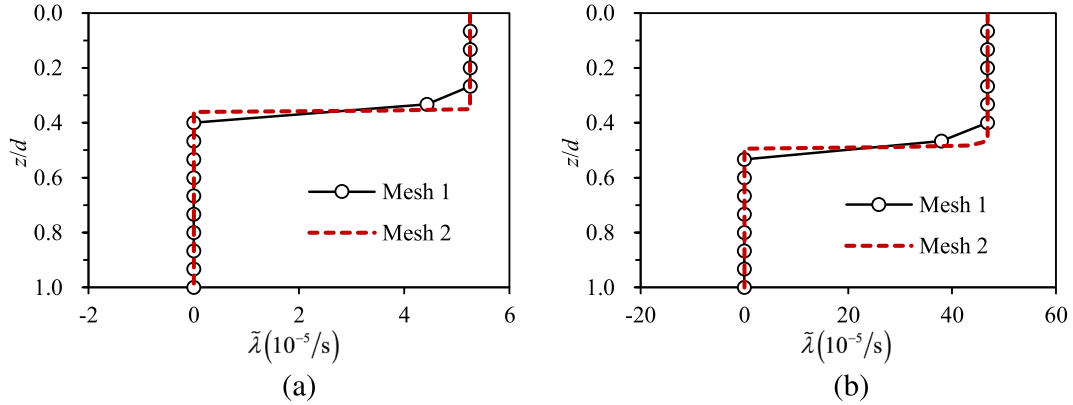

Fig. 16. Vertical distributions of the volume-regularized Lagrange multiplier: (a) 'Test 20' ($S_r = 0.996, t = 0.425T$); and (b) 'Test 2' ($S_r = 0.951, t = 0.45T$).

used, the multiplier will be irregular and the quasi-uniform distribution will be polluted. This will lead to a confusion if we want to explore the physical mechanism in the liquefied zone by investigating the multiplier distribution.

Fortunately, the readily available knowledge in computational contact mechanics tells us a lesson that pointwise KKT condition generally calls for area regularization if the physical meaning of the Lagrange multiplier is crucial. The concept of regularization inspires us to reconsider Eq. (20) which simplifies the integration of the Direct delta function straightforwardly as identity matrices. If the Direct delta function is truly integrated without simplification, then a nodal average volume (V_i) will occur together with the Lagrange multiplier. That is, we should use the volume-regularized Lagrange multiplier: $\widetilde{\lambda} = \lambda/V$. $\widetilde{\lambda}$ has the unit of 1/s, representing the additional volume strain per unit time caused by the fictitious source term λ . The discrete computation of $\widetilde{\lambda}$ can be conducted by:

$$\left[\widetilde{\mathbf{d}}_{\lambda}^{\mathscr{L}}\right]_i = \mathbf{d}_{\lambda}^{\mathscr{L}}/V_i. \tag{31}$$

After the volume regularization, the Lagrange multipliers are plotted in Fig. 16. The results shows that the regularized multipliers given by two meshes are almost the same. Only those points near the liquefaction boundary show some differences. Notably, the volume regularization is only needed when the physical mechanism of the multiplier calls for investigation. Therefore, this technique is actually prepared for future works. In this paper, except for the multiplier results shown in Figs. 15 and 16, other numerical results will not change either using the volume regularization or not.

5.4. Nonlinear convergence performances

The CP model is a linear model wherein no non-linearity is involved. Therefore, the nonlinear convergence performances of DP and NCP are discussed in this section by simulating 'Test 20' and 'Test 2' in Liu et al. (2015). By using 'Mesh 1', Fig. 17 gives the iteration numbers cost by each time step. The liquefaction depth is also shown in Fig. 17 to provide a reference. When the liquefaction occurs, NCP requires only 2–5 iterations to achieve the convergence. In contrast, DP poses apparently more iterations. The NCP treatment proposed in this paper shows a better performance.

If the fine mesh ('Mesh 2') is used, DP is found to cause serious divergences during the iterative procedure. Taking 'Test 2' for an instance, Fig. 18(a) gives the iteration numbers cost by each time step. NCP requires no more than 10 iterations to achieve the convergence. However, if DP is applied, the algorithm diverges at the instant of $t = 0.4T$. At this instant, DP and NCP are compared in Fig. 18(b) with respect to the convergence process. Fig. 18(b) shows that NCP converges within 8 iterations but DP cannot obtain reasonable convergences after 30 iterations.

This behavior is further detailed in Fig. 19 by investigating the L^2-norm of total displacement u and pore pressure p at each iteration. As shown in Fig. 19(a), NCP obtains converged solutions of the displacement u and pore pressure p within 8 iterations. However, no convergence can be expected by using the DP model even after 100 iterations. As shown in Fig. 19(b), DP experiences numerical oscillations and abnormal large values occur during the iterative process. At the 98th iteration, $\|\mathbf{d}_u\|_2$ and $\|\mathbf{d}_p\|_2$ are 30.4 m and 2.1×10^{10} Pa, respectively.

6. 2D wave-seabed interactions

In this section, the present model is further applied to the problem of 2D wave-seabed interactions. Fig. 20 shows the computational mesh for an infinite seabed, wherein the shallow layer and the x-directional central part have smaller element sizes. This setup aims to provide a high numerical accuracy for the potential liquefied zone. The boundary conditions are the same as Fig. 1. The wave parameters and soil properties are identical to those in 'Test 2' (Liu et al., 2015) and are given in Fig. 20. To simulate a seabed with infinite thickness, the thickness of the computational mesh should be larger than the wavelength L (Hsu and Jeng, 1994). Here, $L \approx 61.4$m and the thickness is taken as 100 m. The seabed length is set as three times of the wave length. As reported in Ye and Jeng (2012), such a computational domain is sufficient for the concerned region at the x-directional central part.

In this section, CP, DP and NCP are compared. It is notable that the DP model with the parameters of $c_1 = 100, c_2 = 1$ and $r_u^{\mathrm{cr}} = 1$ is recommended in Section 5 for 1D wave loading but was found leading to numerical instability or divergence in the 2D case, as reported by Zhou et al. (2020b). Then, the DP model (Zhou et al., 2020b) applied the parameters of $c_1 = 10, c_2 = 1$ and $r_u^{\mathrm{cr}} = 1$, which can obtain a converged solution. This group of parameters is therefore also adopted in this section when using the DP model.

As the x-directional central part is the concerned region, all the numerical results in this section are given at the instant of $t = T$ because the position of $x = 1.5L$ is under wave trough at this instant. Fig. 21 shows the contours of $p - P_b$ and $\bar{\sigma}_v'$ by using the CP model. Figs. 22 and 23 are the results given by DP and NCP models, respectively. These three numerical treatments are compared as below.

As shown in Figs. 21(a), 22(a) and 23(a), DP and NCP reduce the value of $(p - P_b)$ under the wave trough, as compared with CP. The reduction by NCP is more significant than DP. This tendency can be seen more clearly in Fig. 24 which plots the vertical distribution of $p - P_b$ at the section of $x = 1.5L$. Fig. 24 also provides the analytical solution (Yamamoto et al., 1978). The results by CP are found agreeing exactly with the analytical solution. This agreement again validates the

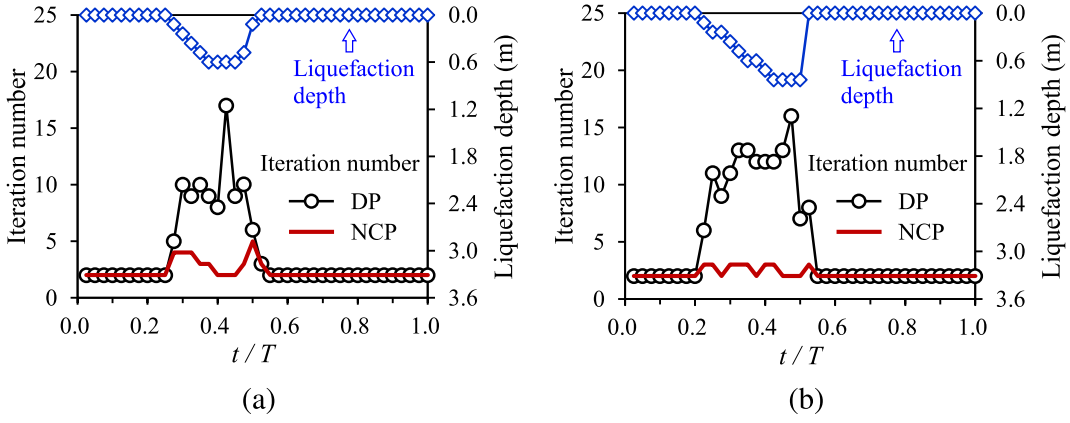

Fig. 17. Iteration number and liquefaction depth versus time step by using 'Mesh 1': (a) 'Test 20' ($S_r = 0.996$); and (b) 'Test 2' ($S_r = 0.951$).

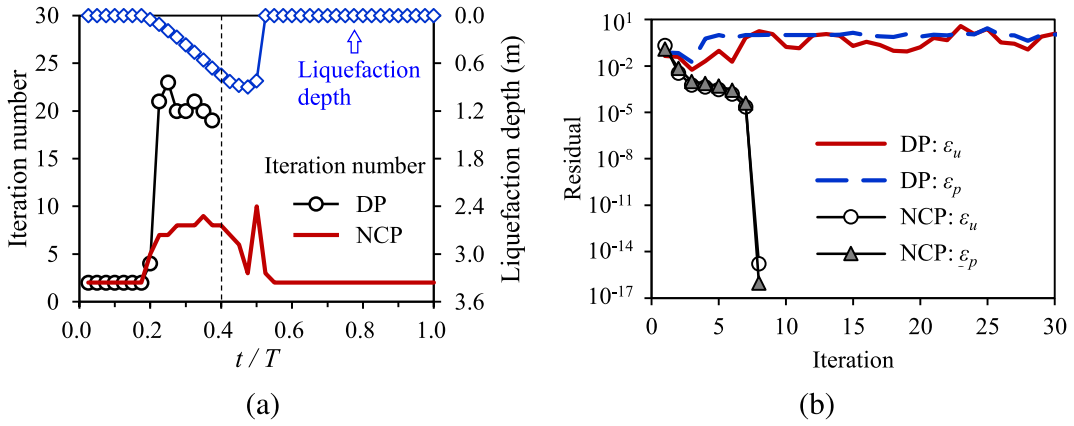

Fig. 18. Nonlinear convergence performances by using 'Mesh 2' to simulate 'Test 2': (a) iteration number and liquefaction depth versus time step; (b) residual at each iteration at $t = 0.4T$.

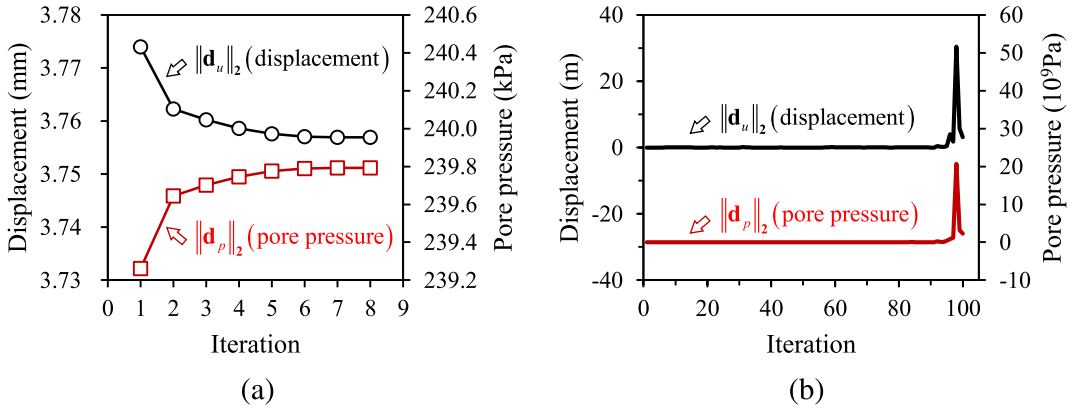

Fig. 19. L^2-norm of total solutions $\|\mathbf{d}_u\|_2$ and $\|\mathbf{d}_p\|_2$ by using 'Mesh 2' to simulate 'Test 2': (a) NCP; (b) DP.

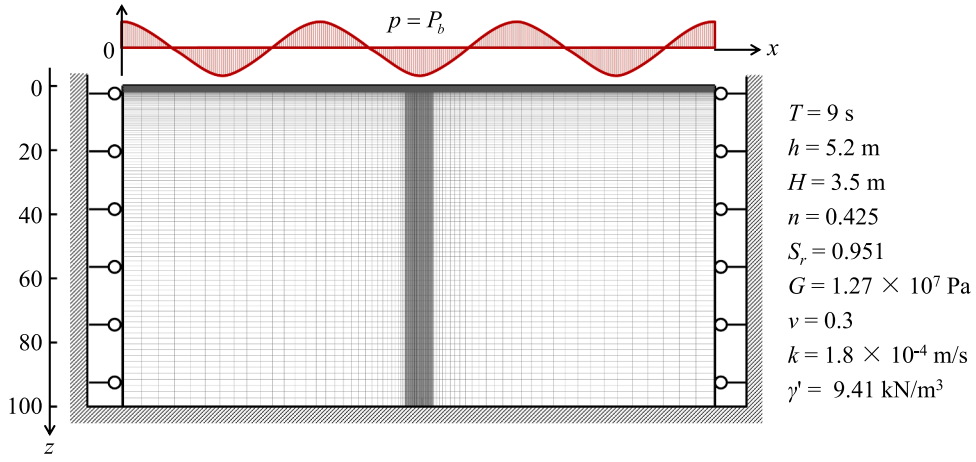

Fig. 20. Computational mesh and boundary conditions of the 2D simulation.

numerical code developed in this paper. According to the reference line ($\gamma' z$) in Fig. 24, CP shows considerable tensile behavior that the wave-induced pore pressure $p - P_b$ exceeds the initial vertical effective stress $\gamma' z$. This unreasonable phenomenon is eased by DP but the tensile behavior is still non-negligible. In contrast, no tensile behavior occurs in the present model (NCP).

The above comparison between $p - P_b$ and $\gamma' z$ (e.g. Fig. 24) is a common treatment in ocean engineering as well as in the field of liquefaction analysis. Here we further provide the contours of the vertical effective stress $\bar{\sigma}'_v$ in Figs. 21(b), 22(b) and 23(b) due to the following two considerations. First, the tensile behavior can be investigated directly in the contours. Second, the isoline of $p_n = 0$ can be used to represent the liquefaction boundary. As shown in Fig. 21(b), the negative values of $\bar{\sigma}'_v$ in CP are rather large. The performances are improved by DP and NCP, as shown in Figs. 22(b) and 23(b). This improvement is further investigated in Fig. 25 by plotting the vertical distribution of $\bar{\sigma}'_v$ at the section of $x = 1.5L$. As shown in Fig. 25, CP

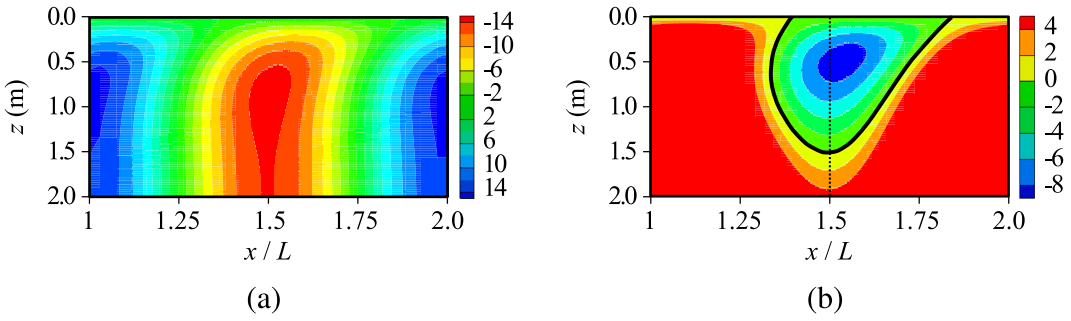

Fig. 21. Numerical results of the 2D simulation by CP: (a) $p - P_b$ (kPa); (b) $\bar{\sigma}'_v$ (kPa).

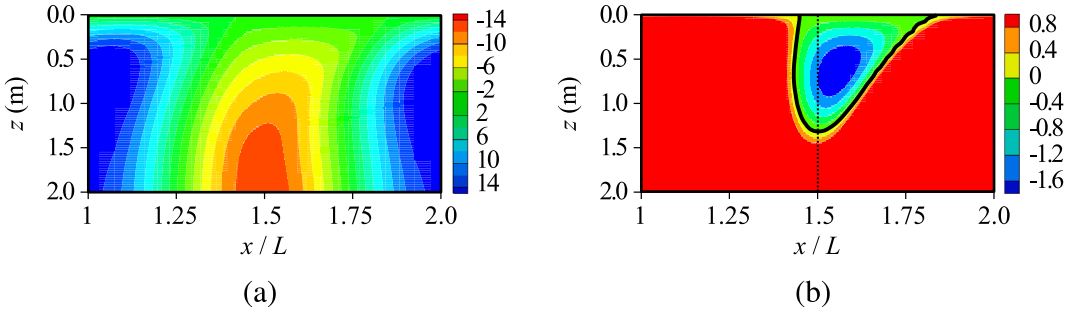

Fig. 22. Numerical results of the 2D simulation by DP: (a) $p - P_b$ (kPa); (b) $\bar{\sigma}'_v$ (kPa).

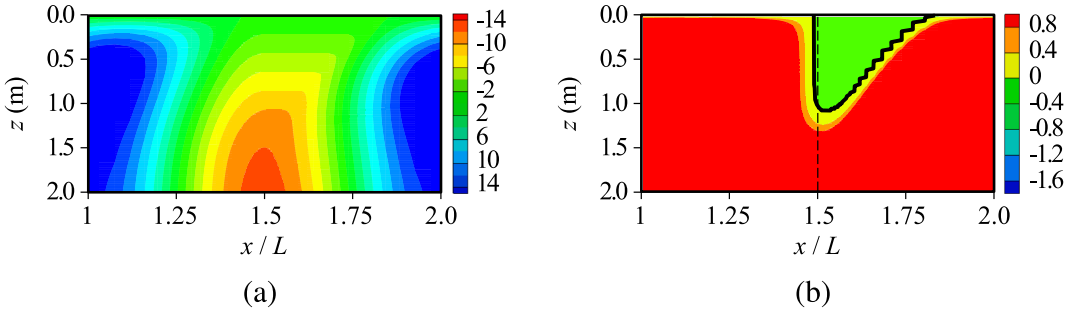

Fig. 23. Numerical results of the 2D simulation by NCP: (a) $p - P_b$ (kPa); (b) $\bar{\sigma}'_v$ (kPa).

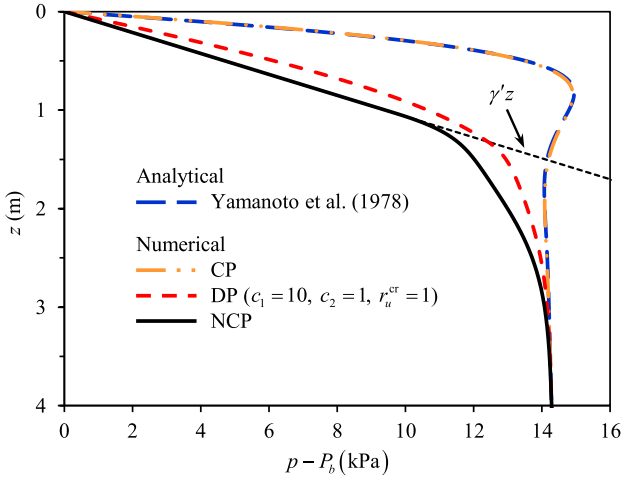

Fig. 24. Vertical distribution of $p - P_b$ in the 2D simulation.

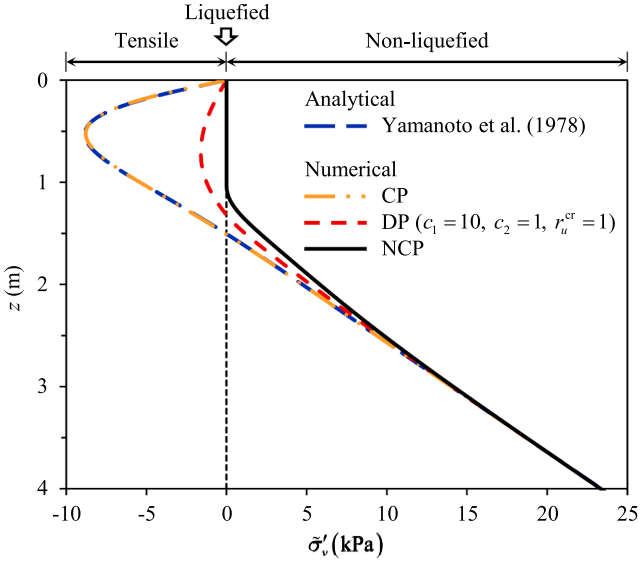

Fig. 25. Vertical distribution of $\bar{\sigma}'_v$ in the 2D simulation.

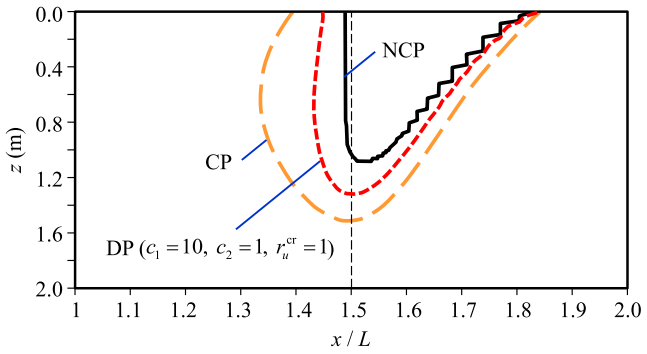

Fig. 26. The liquefied zones given by CP, DP and NCP.

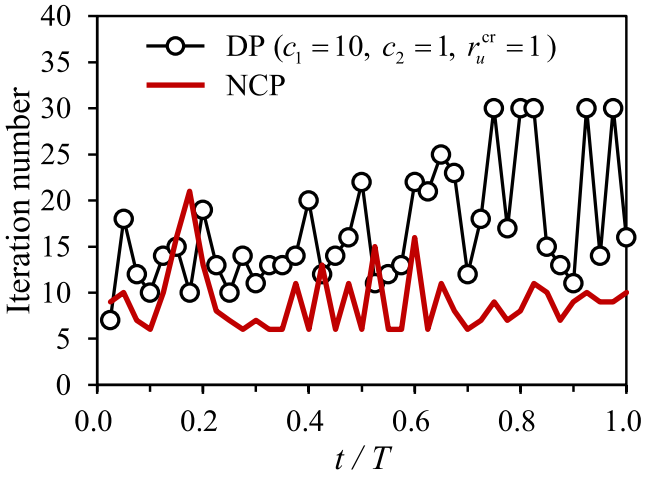

Fig. 27. Iteration number versus time step by using DP and NCP.

obtains a minimum value of $\tilde{\sigma}_v'$ as −9.04 kPa. DP reduces the tensile stress to −2.00 kPa. The improvement by DP is apparent but not thorough. By using the NCP treatment, the numerical results are totally free of unphysical tensile behavior.

The liquefied zones determined in Figs. 21(b), 22(b) and 23(b) are then collected together and are compared in Fig. 26. Based on the above discussion, the result by NCP is reasonable and accurate. Therefore, the comparison between CP and NCP indicates that the conventional Darcy model using constant permeability overestimates the liquefaction potential. The estimation by DP is like an intermediate result from the CP model towards the NCP treatment. A close view of the liquefied zone by NCP shows that the liquefaction boundary is not as smooth as those by CP and DP. Here, this type of non-smoothness is spatial. As discussed in Section 5 for the 1D wave loading, the temporal non-smoothness also occurs in the liquefaction depth. The reason of causing both the temporal and spatial smoothness is the same, i.e. the KKT condition is imposed in a collocation manner. Here we emphasize again that the non-smoothness cannot be attributed to the concept of NCP treatment, because the non-smoothness can be improved by using weak-form KKT conditions in the future which still fall into the framework of NCP treatment.

Fig. 27 compares the iteration number cost by each time step when using DP and NCP. As shown in the comparison, DP requires more iterations to reach the convergence even small 'penalty-like' parameters are used and therefore tensile behavior still occurs. We can conclude that NCP provides better performances in the nonlinear convergence than DP. If we note the fact that large 'penalty-like' parameters in DP lead to algorithm divergence (Zhou et al., 2020b), this conclusion becomes more solid.

7. Conclusions

In this study, we model the wave-induced instantaneous liquefaction in a non-cohesive seabed as a nonlinear complementarity problem (NCP). Compared with the conventional Darcy model using constant permeability, NCP removes the non-physical tensile behavior in a non-cohesive seabed. Compared with the previous dynamic permeability model, NCP needs no extra parameters and achieves superior convergences in the non-linearity treatment. Moreover, the no-tension requirement is precisely fulfilled in NCP, whereas the dynamic permeability model can only partially ease the tensile behavior.

Particularly, the choice of the discrete multiplier space is discussed in details. The Direct delta function is used in the present model to interpolate the multiplier mainly for the sake of minimizing the implementation effort and condensing the multipliers. However, this choice is found to lead to temporal and spatial non-smoothness of the liquefaction boundary. This issue can be eased to some extent by using finer computational meshes and is expected to be addressed by weak-form KKT condition in future works. Nevertheless, numerical investigations indicate that the additional numerical error by using pointwise KKT condition is not significant, and generally we do not need to worry about the accuracy from an engineering point of view.

The primal–dual active strategy is used here to deal with the nonlinearity arising from the NCP. Noting that NCP provides a numerical framework to employ state-of-art methods, the nonlinear convergence can be further improved by using semi-smooth Newton method or interior point method etc. if necessary.

The present work focuses on the simple case of wave-seabed interactions without a structure to highlight the key contributions. This is also fundamental to extend the application to wave-structure-seabed interactions in the future and therefore more complex scenarios with offshore structures can be simulated.

Declaration of Competing Interest

The authors declare that they have no known competing financial interests or personal relationships that could have appeared to influence the work reported in this paper.

Acknowledgements

This work is funded by the Fundamental Research Funds for the Central Universities (Grant No. 2021JBM034); and the National Natural Science Foundation of China (Nos. 51808034 and 11972036).

References

Abdollahi, A., Mason, H.B., 2020. Pore water pressure response during tsunami loading. Journal of Geotechnical and Geoenvironmental Engineering, ASCE 146, 04020004. https://doi.org/10.1061/(ASCE)GT.1943-5606.0002205.

Adamidis, O., Madabhushi, G., 2016. Post-liquefaction reconsolidation of sand. In: Proceedings of the Royal Society A: Mathematical, Physical and Engineering Sciences. https://doi.org/10.1098/rspa.2015.0745, 472.

Arulanandan, K., Sybico Jr, J., 1992. Post-liquefaction settlement of sand. The Wroth Memorial Symposium 94–110.

Belytschko, T., Black, T., 1999. Elastic crack growth in finite elements with minimal remeshing. Int. J. Numer. Meth. Eng. 45, 601–620. https://doi.org/10.1002/(SICI)1097-0207(19990620)45:5<601::AID-NME598>3.0.CO;2-S.

Biot, M.A., 1941. General theory of three-dimensional consolidation. J. Appl. Phys. 26, 155–164.

Celli, D., Li, Y., Ong, M.C., Di Risio, M., 2019. The role of submerged berms on the momentary liquefaction around conventional rubble mound breakwaters. Appl. Ocean Res. 85, 1–11. https://doi.org/10.1016/j.apor.2019.01.023.

Chen, R., Wu, L., Zhu, B., Kong, D., 2019. Numerical modelling of pipe-soil interaction for marine pipelines in sandy seabed subjected to wave loadings. Appl. Ocean Res. 88, 233–245. https://doi.org/10.1016/j.apor.2019.04.021.

Chen, W., Liu, C., Li, Y., Chen, G., Jeng, D., Liao, C., Yu, J., 2020. An integrated numerical model for the stability of artificial submarine slope under wave load. Coast. Eng. 158, 103698. https://doi.org/10.1016/j.coastaleng.2020.103698.

Cuéllar, P., Mira, P., Pastor, M., Fernandez Merodo, J.A., Baessler, M., Ruecker, W., 2014. A numerical model for the transient analysis of offshore foundations under cyclic

loading. Comput. Geotech. 59, 75–86. https://doi.org/10.1016/j.compgeo.2014.02.005.
Dean, R., Dalrymple, R.A., 1984. Water wave mechanics for engineers and scientists. World Scientific.
Duan, L., Jeng, D.S., Wang, D., 2019. PORO-FSSI-FOAM: Seabed response around a mono-pile under natural loadings. Ocean Eng. 184, 239–254. https://doi.org/10.1016/j.oceaneng.2019.05.024.
Duan, L., Liao, C., Jeng, D.S., Chen, L., 2017. 2D numerical study of wave and current-induced oscillatory non-cohesive soil liquefaction around a partially buried pipeline in a trench. Ocean Eng. 135, 39–51. https://doi.org/10.1016/j.oceaneng.2017.02.036.
Elsafti, H., Oumeraci, H., 2016. A numerical hydro-geotechnical model for marine gravity structures. Comput. Geotech. 79, 105–129. https://doi.org/10.1016/j.compgeo.2016.05.025.
Gao, F., Jeng, D., Sekiguchi, H., 2003. Numerical study on the interaction between non-linear wave, buried pipeline and non-homogenous porous seabed. Comput. Geotech. 30, 535–547. https://doi.org/10.1016/S0266-352X(03)00053-3.
Ha, I., Park, Y., Kim, M., 2003. Dissipation pattern of excess pore pressure after liquefaction in saturated sand deposits, in: Geology and Properties of Earth Materials 2003: Soils, Geology, and Foundations, pp. 59–67.
Haigh, S.K., Eadington, J., Madabhushi, S.P.G., 2012. Permeability and stiffness of sands at very low effective stresses. Géotechnique 62, 69–75. https://doi.org/10.1680/geot.10.P.035.
Han, S., Jeng, D.S., Tsai, C.C., 2019. Response of a porous seabed around an immersed tunnel under wave loading: Meshfree model. Journal of Marine Science and Engineering 7, 369. https://doi.org/10.3390/jmse7100369.
Hsu, J., Jeng, D.S., 1994. Wave-induced soil response in an unsaturated anisotropic seabed of finite thickness. Int. J. Numer. Anal. Meth. Geomech. 18, 785–807. https://doi.org/10.1002/nag.1610181104.
Jeng, D.S., 1997. Wave-induced seabed instability in front of a breakwater. Ocean Eng. 24, 887–917. https://doi.org/10.1016/S0029-8018(96)00046-7.
Jeng, D.S., 2012. Porous models for wave-seabed interaction. Springer. https://doi.org/10.1007/978-3-642-33593-8.
Jeng, D.S., 2018. Mechanics of wave-seabed-structure interactions: modelling, processes and applications. Cambridge University Press. https://doi.org/10.1017/9781316672266.
Jeng, D.S., Lin, Y., 1999. Wave–induced pore pressure around a buried pipeline in gibson soil: finite element analysis. Int. J. Numer. Anal. Meth. Geomech. 23, 1559–1578. https://doi.org/10.1002/(SICI)1096-9853(199911)23:13<1559::AID-NAG57>3.0.CO;2-U.
Jeng, D.S., Ou, J., 2010. 3D models for wave-induced pore pressures near breakwater heads. Acta Mech. 215, 85–104. https://doi.org/10.1007/200707-010-0303-z.
Jeng, D.S., Seymour, B., Li, J., 2007. A new approximation for pore pressure accumulation in marine sediment due to water waves. Int. J. Numer. Anal. Meth. Geomech. 31, 53–69. https://doi.org/10.1002/nag.547.
Jeng, D.S., Zhao, H.Y., 2015. Two-dimensional model for accumulation of pore pressure in marine sediments. Journal of Waterway, Port, Coastal, and Ocean Engineering, ASCE 141, 04014042. https://doi.org/10.1061/(ASCE)WW.1943-5460.0000282.
Kudella, M., Oumeraci, H., de Groot, M., Meijers, P., 2006. Large-scale experiments on pore pressure generation underneath a caisson breakwater. Journal of Waterways, Port, Coastal and Ocean Engineering, ASCE 132, 310–324. https://doi.org/10.1061/(ASCE)0733-950X(2006)132:4(310).
Kunisch, K., RöSch, A., 2002. Primal-dual active set strategy for a general class of constrained optimal control problems. Siam Journal on Optimization 13, 321–334. https://doi.org/10.1137/S1052623499358008.
Li, K., Guo, Z., Wang, L., Jiang, H., 2019. Effect of seepage flow on shields number around a fixed and sagging pipeline. Ocean Eng. 172, 487–500. https://doi.org/10.1016/j.oceaneng.2018.12.033.
Li, Y., Ong, M.C., Tang, T., 2018. Numerical analysis of wave-induced poro-elastic seabed response around a hexagonal gravity-based offshore foundation. Coast. Eng. 136, 81–95. https://doi.org/10.1016/j.coastaleng.2018.02.005.
Liang, Z., Jeng, D.S., Liu, J., 2020. Combined wave–current induced seabed liquefaction around buried pipelines: Design of a trench layer. Ocean Eng. 212, 107764. https://doi.org/10.1016/j.oceaneng.2020.107764.
Liao, C.C., Chen, J.J., Zhang, Y.Z., 2019. Accumulation of pore water pressure in a homogeneous sandy seabed around a rocking mono-pile subjected to wave loads. Ocean Eng. 173, 810–823. https://doi.org/10.1016/j.oceaneng.2018.12.072.
Lin, Z., Pokrajac, D., Guo, Y., Jeng, D.S., Tang, T., Rey, N., Zheng, J., Zhang, J., 2017. Investigation of nonlinear wave-induced seabed response around mono-pile foundation. Coast. Eng. 121, 197–211. https://doi.org/10.1016/j.coastaleng.2017.01.002.
Liu, B., Jeng, D.S., Ye, G., Yang, B., 2015. Laboratory study for pore pressures in sandy deposit under wave loading. Ocean Eng. 106, 207–219. https://doi.org/10.1016/j.oceaneng.2015.06.029.
Madsen, O.S., 1978. Wave-induced pore pressures and effective stresses in a porous bed. Géotechnique 28, 377–393. https://doi.org/10.1680/geot.1978.28.4.377.
Michallet, H., Mory, M., Piedra-Cueva, I., 2009. Wave-induced pore pressure measurements near a coastal structure. Journal of Geophysical Research (Oceans) 114, C06019. https://doi.org/10.1029/2008JC005071.
Miyamoto, J., Sassa, S., Sekiguchi, H., 2004. Progressive solidification of a liquefied sand layer during continued wave loading. Géotechnique 54, 617–629. https://doi.org/10.1680/geot.54.10.617.56343.
Moës, N., Dolbow, J., Belytschko, T., 1999. A finite element method for crack growth without remeshing. Int. J. Numer. Meth. Eng. 46, 131–150. https://doi.org/10.1002/(SICI)1097-0207(19990910)46:1<131::AID-NME726>3.3.CO;2-A.
Okusa, S., 1985. Wave-induced stress in unsaturated submarine sediments. Géotechnique 35, 517–532.
Qi, W.G., Gao, F.P., 2014. Physical modelling of local scour development around a large-diameter monopile in combined waves and current. Coast. Eng. 83, 72–81. https://doi.org/10.1016/j.coastaleng.2013.10.007.
Qi, W.G., Gao, F.P., 2015. A modified criterion for wave-induced momentary liquefaction of sandy seabed. Theoretical & Applied Mechanics Letters 5, 20–23.
Qi, W.G., Gao, F.P., 2018. Wave induced instantaneously-liquefied soil depth in a non-cohesive seabed. Ocean Eng. 153, 412–423. https://doi.org/10.1016/j.oceaneng.2018.01.107.
Qi, W.G., Shi, Y.M., Gao, F.P., 2020. Uplift soil resistance to a shallowly-buried pipeline in the sandy seabed under waves: Poro-elastoplastic modeling. Appl. Ocean Res. 95, 102024. https://doi.org/10.1016/j.apor.2019.102024.
Sassa, S., Sekiguchi, H., 2001. Analysis of wave-induced liquefaction of sand beds. Géotechnique 51, 115–126.
Seed, H.B., Lysmer, J., Martin, P.P., 1976. Pore-water pressure changes during soil liquefaction. Journal of Geotechnical Engineering Division, ASCE 102, 323–346.
Seed, H.B., Rahman, M.S., 1978. Wave-induced pore pressure in relation to ocean floor stability of cohesionless soils. Mar. Geotechnol. 3, 123–150.
Shahir, H., Mohammadi-Haji, B., Ghassemi, A., 2014. Employing a variable permeability model in numerical simulation of saturated sand behavior under earthquake loading. Comput. Geotech. 55, 211–223. https://doi.org/10.1016/j.compgeo.2013.09.007.
Sui, T., Zhang, C., Guo, Y., Zheng, J., Jeng, D.S., Zhang, J., Zhang, W., 2016. Three-dimensional numerical model for wave-induced seabed response around mono-pile. Ships and Offshore Structures 11, 667–678. https://doi.org/10.1080/17445302.2015.1051312.
Sumer, B.M., 2014. Liquefaction around Marine Structures. World Scientific, New Jersey.
Sumer, B.M., Fredsøe, J., 2002. The Mechanics of scour in the marine environment. World Scientific.
Sumer, B.M., Hatipoglu, F., Fredsøe, J., Sumer, S.K., 2006. The sequence of sediment behaviour during wave-induced liquefaction. Sedimentology 53, 611–629. https://doi.org/10.1111/j.1365-3091.2006.00763.x.
Sumer, B.M., Kirca, V.S.O., Fredsøe, J., 2012. Experimental validation of a mathematical model for seabed liquefaction under waves. Int. J. Offshore Polar Eng. 22, 133–141.
Sumer, S., Sumer, B., Dixen, F., Fredsøe, J., 2008. Pore pressure buildup in the subsoil under a caisson breakwater. In: In the Eighteenth International Offshore and Polar Engineering Conference. International Society of Offshore and Polar Engineers, pp. 664–671.
Tian, R., Wen, L., Wang, L., 2019. Three-dimensional improved XFEM (IXFEM) for static crack problems. Comput. Methods Appl. Mech. Eng. 343, 339–367. https://doi.org/10.1016/j.cma.2018.08.029.
Tonkin, S., Yeh, H., Kato, F., Sato, S., 2003. Tsunami scour around a cylinder. J. Fluid Mech. 496, 165–192. https://doi.org/10.1017/S0022112003006402.
Ueng, T.S., Wang, Z.F., Chu, M.C., Ge, L., 2017. Laboratory tests for permeability of sand during liquefaction. Soil Dynamics and Earthquake Engineering 100, 249–256. https://doi.org/10.1016/j.soildyn.2017.05.037.
Verruijt, A., 1969. Elastics storage of aqifers. Flow through Porous Media. Academic Press 331–376.
Wang, B., Zen, K., Chen, G.Q., Zhang, Y.B., Kasama, K., 2013. Excess pore pressure dissipation and solidification after liquefaction of saturated sand deposits. Soil Dynamics and Earthquake Engineering 49, 157–164. https://doi.org/10.1016/j.soildyn.2013.02.018.
Wang, R., Zhang, J.M., Wang, G., 2014. A unified plasticity model for large post-liquefaction shear deformation of sand. Comput. Geotech. 59, 54–66. https://doi.org/10.1016/j.compgeo.2014.02.008.
Wang, W., Zhou, M., Zhang, B., Peng, C., 2019. A dual mortar contact method for porous media and its application to clay-core rockfill dams. Int. J. Numer. Anal. Meth. Geomech. 43, 1744–1769. https://doi.org/10.1002/nag.2930.
Wriggers, P., 2006. Computational contact mechanics, 2nd edn. Springer, Berlin.
Wu, S., Jeng, D.S., 2019. Effects of dynamic soil permeability on the wave-induced seabed response around a buried pipeline. Ocean Eng. 186, 106132. https://doi.org/10.1016/j.oceaneng.2019.106132.
Wu, S., Jeng, D.S., Seymour, B., 2020. Numerical modelling of consolidation-induced solute transport in unsaturated soil with dynamic hydraulic conductivity and degree of saturation. Adv. Water Resour. 135, 103466. https://doi.org/10.1016/j.advwatres.2019.103466.
Yamamoto, T., Koning, H., Sellmeijer, H., Hijum, E.V., 1978. On the response of a poro-elastic bed to water waves. J. Fluid Mech. 87, 193–206. https://doi.org/10.1017/S0022112078003006.
Ye, J., Jeng, D.S., 2012. Response of porous seabed to nature loadings: Waves and currents. Journal of Engineering Mechanics, ASCE 138, 601–613. https://doi.org/10.1061/(ASCE)EM.1943-7889.0000356.
Ye, J., Jeng, D.S., Wang, R., Zhu, C., 2015. Numerical simulation of the wave-induced dynamic response of poro-elastoplastic seabed foundations and a composite breakwater. Appl. Math. Model. 39, 322–347. https://doi.org/10.1016/j.apm.2014.05.031.
Yeh, H., Mason, H.B., 2014. Sediment response to tsunami loading: mechanisms and estimates. Géotechnique 64, 131–143. https://doi.org/10.1680/geot.13.P.033.
Zen, K., Yamazaki, H., 1990. Mechanism of wave-induced liquefaction and densification in seabed. Soils Found. 30, 90–104. https://doi.org/10.3208/sandf1972.30.4_90.
Zhang, J., Tong, L., Zheng, J., He, R., Guo, Y., 2018. Effects of soil-resistance damping on wave-induced pore pressure accumulation around a composite breakwater. J. Coastal Res. 34, 573–585. https://doi.org/10.2112/JCOASTRES-D-17-00033.1.
Zhang, Y., Jeng, D.S., Gao, F., Zhang, J.S., 2013. An analytical solution for response of a porous seabed to combined wave and current loading. Ocean Eng. 57, 240–247. https://doi.org/10.1016/j.oceaneng.2012.09.001.

Zhao, H.Y., Jeng, D.S., 2016. Accumulated pore pressures around submarine pipeline buried in trench layer with partial backfills. Journal of Engineering Mechanics, ASCE 142, 04016042. https://doi.org/10.1061/(ASCE)EM.1943-7889.0001093.

Zheng, H., Liu, F., Du, X., 2015. Complementarity problem arising from static growth of multiple cracks and mls-based numerical manifold method. Comput. Methods Appl. Mech. Eng. 295, 150–171. https://doi.org/10.1016/j.cma.2015.07.001.

Zheng, H., Zhang, T., Wang, Q., 2020. The mixed complementarity problem arising from non-associative plasticity with non-smooth yield surfaces. Comput. Methods Appl. Mech. Eng. 361, 112756. https://doi.org/10.1016/j.cma.2019.112756.

Zhou, M., Zhang, B., Chen, T., Peng, C., Fang, H., 2020a. A three-field dual mortar method for elastic problems with nonconforming mesh. Comput. Methods Appl. Mech. Eng. 362, 112870. https://doi.org/10.1016/j.cma.2020.112870.

Zhou, M., Zhang, B., Peng, C., 2018. Numerical evaluation of soft inter-slab joint in concrete-faced rockfill dam with dual mortar finite element method. Int. J. Numer. Anal. Meth. Geomech. 42, 781–805. https://doi.org/10.1002/nag.2768.

Zhou, M.Z., Jeng, D.S., Qi, W.G., 2020b. A new model for wave-induced instantaneous liquefaction in a non-cohesive seabed with dynamic permeability. Ocean Eng. 213, 107597. https://doi.org/10.1016/j.oceaneng.2020.107597.

Zhou, X.L., Zhang, J., Wang, J.H., Xu, Y.F., Jeng, D.S., 2014. Stability and liquefaction analysis of porous seabed subjected to cnoidal wave. Appl. Ocean Res. 48, 250–265. https://doi.org/10.1016/j.apor.2014.09.005.